Article

Structural basis of lipid transfer by a bridge-like lipid-transfer protein

https://doi.org/10.1038/s41586-025-08918-y

Received: 21 June 2024

Accepted: 19 March 2025

Published online: 23 April 2025

Check for updates

Yunsik Kang[1,2], Katherine S. Lehmann[1], Hannah Long[3], Amanda Jefferson[1], Maria Purice[3,4], Marc Freeman[1] & Sarah Clark[3]✉

Bridge-like lipid-transport proteins (BLTPs) are an evolutionarily conserved family of proteins that localize to membrane-contact sites and are thought to mediate the bulk transfer of lipids from a donor membrane, typically the endoplasmic reticulum, to an acceptor membrane, such as that of the cell or an organelle[1]. Although BLTPs are fundamentally important for a wide array of cellular functions, their architecture, composition and lipid-transfer mechanisms remain poorly characterized. Here we present the subunit composition and the cryogenic electron microscopy structure of the native LPD-3 BLTP complex isolated from transgenic *Caenorhabditis elegans*. LPD-3 folds into an elongated, rod-shaped tunnel of which the interior is filled with ordered lipid molecules that are coordinated by a track of ionizable residues that line one side of the tunnel. LPD-3 forms a complex with two previously uncharacterized proteins, one of which we have named Spigot and the other of which remains unnamed. Spigot interacts with the N-terminal end of LPD-3 where lipids are expected to enter the tunnel, and experiments in multiple model systems indicate that Spigot has a conserved role in BLTP function. Our LPD-3 complex structural data reveal protein–lipid interactions that suggest a model for how the native LPD-3 complex mediates bulk lipid transport and provides a foundation for mechanistic studies of BLTPs.

Cells and cellular organelles are encircled by membranes that each contain a characteristic lipid composition[2]. These membranes are not static structures, but are constantly undergoing dynamic modification as a result of cellular processes such as autophagy, phagocytosis, exocytosis and organelle biosynthesis or even changing environmental conditions (such as temperature). The majority of cellular lipids are synthesized in the endoplasmic reticulum (ER) and, as lipids cannot efficiently diffuse through the aqueous cytosolic environment, they are delivered to other cellular compartments through vesicular or non-vesicular transport[3,4]. Non-vesicular lipid transport is carried out by lipid-transport proteins (LTPs), cytoplasmic proteins that contain a hydrophobic core that shelters lipids from the aqueous environment during transport[5]. LTPs are found mainly at membrane-contact sites, such as those between the ER and the plasma membrane (PM), and most known LTPs operate by shuttling one to four lipid molecules at a time from the donor to acceptor membrane[5,6]. By contrast, the recently identified bridge-like LPTs (BLTPs) are believed to function as molecular bridges that span the distance between the ER and membranes targeted for lipid delivery, enabling the solubilization and transport of large volumes of lipids[1,7]. Structural evidence[8–10] and AlphaFold predictions[1] indicate that BLTPs fold into a rod-like tunnel with a hydrophobic lining that is formed by a series of repeating β-groove (RBG) domains, a defining feature of the BLTP superfamily.

Mutations in human BLTP1 are linked to Alkuraya–Kučinskas syndrome, a devastating neurological disorder[11], but the cellular and molecular basis of this syndrome is not understood. BLTP1 family members are found in all eukaryotes and have been demonstrated to localize to ER–PM contact sites in both yeast and worms[12,13]. Multiple lines of evidence support the notion that BLTP1 and its orthologues function as molecular bridges for lipid transport at ER–PM contact sites: in yeast, the BLTP1 orthologue (Csf1) is important for growth at low temperatures and homeoviscous membrane adaptation[12,14,15]; in *Drosophila*, the BLTP1 orthologue (Tweek) is required for development, synaptic vesicle recycling[16] and astrocyte-mediated phagocytosis of neuronal debris[17]; and, in *C. elegans*, the BLTP1 orthologue (LPD-3) is critical for worm development, efficient phagocytosis and adaptation to cold stress[13,17].

While it is believed that the primary function of BLTP1 family members is bulk transfer of lipids from the ER to the PM, the mechanisms of lipid uptake and transfer, regulation of lipid transport and potential additional roles for BLTPs in vivo remain undefined. All BLTP1 orthologues have a very high molecular mass—LPD-3 and Tweek are the 32nd and 23rd largest proteins in the worm and fly genomes, respectively—and their enormous size has hindered structural and biochemical analysis owing to difficulties associated with recombinant production of full-length protein[18]. Here we overcome these challenges by isolating the native LPD-3 complex from transgenic *C. elegans*. Single-particle cryogenic electron microscopy (cryo-EM) reconstructions and mass spectrometry (MS) analyses reveal the subunit composition and structural details of the native LPD-3 complex, including its interaction with

[1]Vollum Institute, Oregon Health & Science University, Portland, OR, USA. [2]Department of Cell and Developmental Biology, University of Colorado School of Medicine, Aurora, CO, USA. [3]Department of Biochemistry and Biophysics, Oregon State University, Corvallis, OR, USA. [4]Division of Basic Sciences, Fred Hutchinson Cancer Center, Seattle, WA, USA. ✉e-mail: clarksar@oregonstate.edu

27 lipid molecules that fill the modelled portion of the hydrophobic LPD-3 tunnel and three that are associated with the transmembrane domain. We present a model for the structural basis of LPD-3-mediated lipid transfer between membranes that is based on the organization and interactions of these lipid molecules within the LPD-3 tunnel.

Isolation of the native LPD-3 complex

To enable isolation of the native LPD-3 complex, we designed two transgenic worm lines in which DNA encoding an mVenus fluorophore and a 3×Flag tag were inserted either at the start or the end of the endogenous *lpd-3* gene. We refer to these as the *mvenus::lpd3* and *lpd3::mvenus* worm lines, which produce N- and C-terminally tagged LPD-3 protein, respectively. To determine whether insertion of the tag at either position disrupts LPD-3 protein function in the transgenic worms, we compared the development rates and cold tolerance of the transgenic worm lines to that of wild-type (WT) N2 worms[13]. We found that the C-terminally tagged *lpd3::mvenus* worms and WT worms developed at approximately the same rate, with more than 90% of both reaching the L4 developmental stage by 40 h (Extended Data Fig. 1a). The *lpd3::mvenus* worms and WT worms also exhibited a similar resilience to cold exposure, with around 70% of both worm populations surviving after 12 h at 4 °C, consistent with previous results[13] (Extended Data Fig. 1b). By contrast, only 14% of N-terminally tagged *mvenus::lpd3* worms reached the L4 stage by 40 h and only 39% survived cold exposure, indicating impaired LPD-3 function. The C-terminally tagged *lpd3::mvenus* worm line was therefore selected for downstream structural and biochemical experiments. Further characterization of the *lpd3::mvenus* worm line by spectral confocal imaging revealed a pattern of mVenus fluorescence that was consistent with previously reported images of tagged-LPD-3[13] (Extended Data Fig. 2a).

Next, using our recently developed protocol for isolating native membrane protein complexes from *C. elegans*[19], the C-terminally tagged LPD-3 complex was isolated from *lpd3::mvenus* worms (Extended Data Fig. 2). During purification, fluorescence-based size-exclusion chromatography (FSEC) gave a monodisperse peak with an estimated molecular mass of 750 kDa (Extended Data Fig. 2b). As this value exceeds the expected 483 kDa size of tagged LPD-3, this implies that the complex has additional subunits.

To determine the subunit composition of the LPD-3 complex, we performed MS analyses (Extended Data Fig. 2d). The MS results contained peptides that spanned the entire 4,022-residue LPD-3 protein, indicating that the isolated protein was intact. In addition to the LPD-3 peptides, two proteins stood out in terms of their high peptide spectral counts and appeared to have co-purified with LPD-3. We have named one of them Spigot (encoded by *spgt-1*) based its location in the cryo-EM structure (see below) and the other remains unnamed due to ambiguity surrounding its location in the cryo-EM structure and its role in lipid transfer. In this text, we refer to the second protein as 'lipid transfer auxiliary protein 2' (LTAP2). These are both previously uncharacterized proteins, although the human orthologue of Spigot, C1orf43, was identified along with BLTP1 in a genome-wide CRISPR screen as a regulator of phagocytosis of *Legionella pneumophila* in macrophages[20]. Neither Spigot nor LTAP2 was observed in an identically prepared sample from WT N2 worms, demonstrating that these proteins specifically associate with LPD-3.

Sequence-alignment searches revealed that Spigot and LTAP2 are widely conserved across the animal kingdom. Spigot exhibits a level of sequence conservation roughly matching that of LPD-3 with its orthologues, sharing approximately 15–20% sequence identity with the *Drosophila melanogaster* and human orthologues. Notably, Spigot and its orthologues are predicted to be ER-resident proteins, as assessed by the program ERPred[21]. LTAP2 shares 12–18% sequence identity with the *D. melanogaster* and human orthologues and is not predicted to be an ER-resident protein.

Further inspection of the MS analyses revealed 11 additional proteins that exhibit much lower peptide spectral counts compared with Spigot and LTAP2 yet show a strong contrast with the control sample from WT worms (Extended Data Fig. 3a). To investigate the possibility that these proteins functionally interact with LPD-3 complex in vivo (for example, transiently or by binding to a subset), we assayed the ability of astrocytes to phagocytose neuronal debris during developmental neuronal remodelling, a recently identified role for *Drosophila* Tweek (Tweek is the LPD-3 orthologue)[17]. We found that astrocyte-specific RNA interference (RNAi) knockdown of Spigot and LTAP2 resulted in considerable defects in astrocyte phagocytic function (Extended Data Fig. 3). Furthermore, 9 out of the 11 additional proteins that co-purified with the LPD-3 complex also exhibited phagocytosis defects, supporting the notion that the majority of these proteins may have a role in BLTP1 complex function in vivo.

Architecture of the LPD-3 complex

To elucidate the architecture of the native, C-terminally tagged LPD-3 complex, we performed single-molecule cryo-EM analysis of the purified complex. We initially obtained a map of the complex at a nominal resolution of 2.7 Å that corresponds to the N-terminal half of LPD-3 (Extended Data Figs. 4 and 5 and Extended Data Table 1). In an effort to resolve the entire 4,022-residue protein, we selected particles with strong density features for the C-terminal portion of the protein and obtained a full-length map at a nominal resolution of 6.2 Å (Extended Data Fig. 6). We suspect that the inability to obtain a high-resolution map of the C-terminal half of LPD-3, residues 1680–4022, is due to conformational heterogeneity in that half of the protein. Notably, the starting point of the heterogeneity matches the location of a 115-residue segment—residues 1680–1794—that is predicted to be intrinsically disordered, and the C-terminal half of LPD-3 is predicted to contain 8 loops, from 37 to 71 residues long, that are also predicted to be disordered.

The full-length map measures around 345 Å at its longest axis, which matches the expected size of LPD-3, on the basis of AlphaFold2 predictions (Extended Data Fig. 6). Density corresponding to a detergent micelle is observed at one end of the full-length map, indicating the presence of a transmembrane domain, and a tunnel is observed along the length of the entire protein (Extended Data Fig. 6b). These features are consistent with predicted BLTP1 models that contain a single N-terminal transmembrane helix[1], as well as with low-resolution cryo-EM maps of BLTP family members Vps13 (ref. 8), SHIP164 (ref. 9) and Atg2 (ref. 22).

The N-terminal map enabled us to build a model of LPD-3 residues 21–1679 and Spigot residues 7–187, along with 30 well-resolved lipid molecules (Fig. 1). We also observed three additional α-helical densities in the transmembrane domain that remain uninterpreted. LPD-3 begins with a single transmembrane helix, followed by an elongated, tube-shaped structure with an internal cavity. The protein fold is consistent with experimental structures of recombinantly expressed proteins[8–10,23,24] and predicted models[1,25] of BLTP family members (Extended Data Fig. 7). The LPD-3 tunnel is positioned at approximately a 40° angle relative to the membrane bilayer and is filled with an abundance of well-resolved phospholipids. Spigot extends approximately 70 Å across the exterior surface of LPD-3, beginning with its transmembrane helix and terminating with an irregular four-helix bundle (helices H2 to H5) that is nested on the surface of LPD-3 (Fig. 1a,b). As Spigot is a predicted ER-resident protein, its location reinforces existing evidence[13] that LPD-3 is N-terminally anchored to the ER. Given that assumption, this structure provides a view of the site where lipids enter the tunnel for transport to the PM. The uninterpreted density, located on the opposite side of LPD-3 transmembrane helix 1 (TM1) from Spigot, appears to be a three-helix transmembrane bundle from one or two proteins of unknown identity (Fig. 1a). Importantly, TM2 of the density feature, along with LPD-3 TM1, create a surface within the membrane that leads to the entrance to the lipid-transport tunnel.

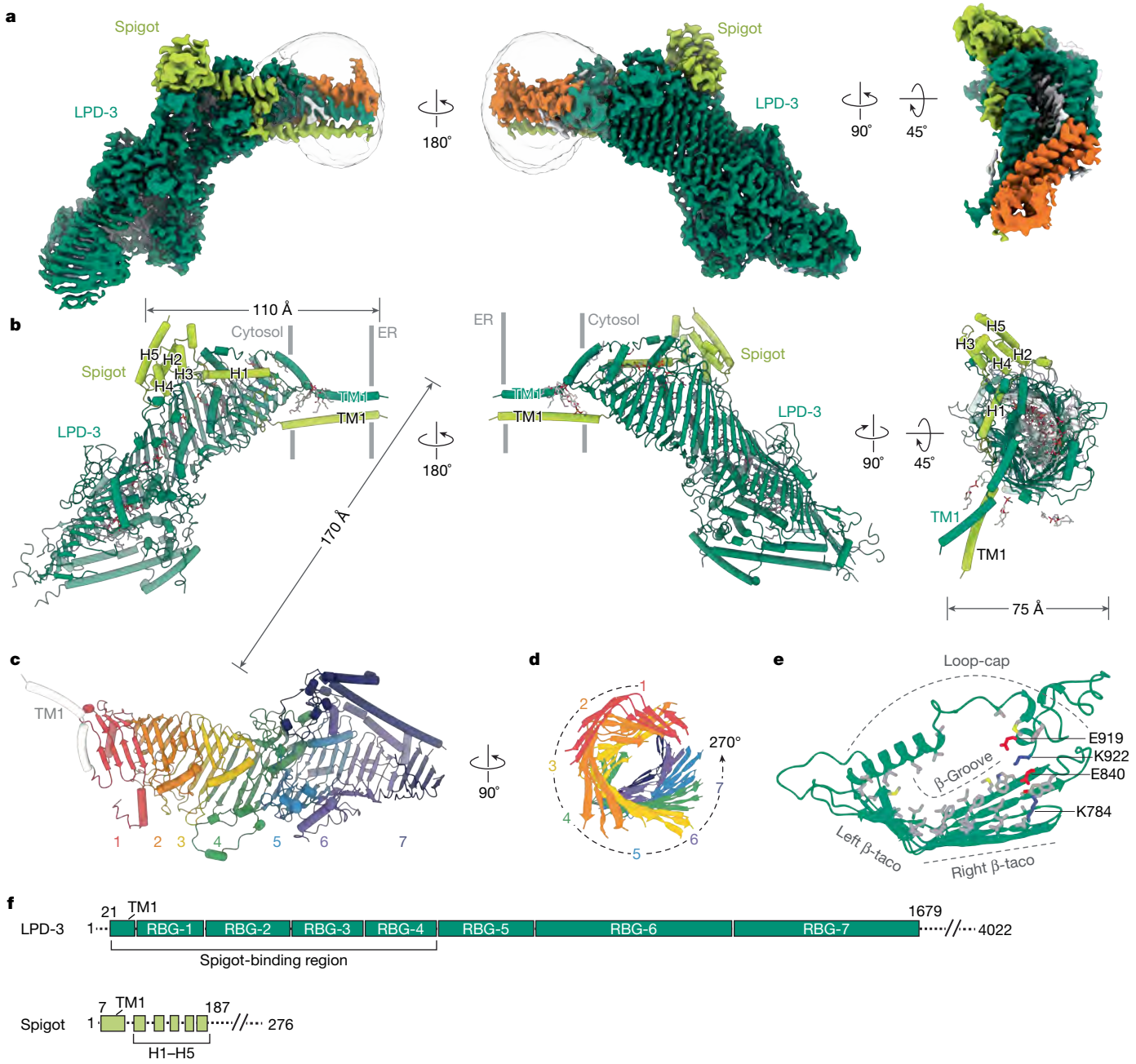

Fig. 1 | The architecture of the LPD-3 complex. a, Cryo-EM map of the native LPD-3 complex shown parallel to the membrane and perpendicular to the membrane. LPD-3 is coloured teal, Spigot is coloured yellow, lipid molecules are coloured light grey and the uninterpreted density feature that corresponds to one or two auxiliary proteins is coloured orange. **b**, Model of the native LPD-3 complex, shown in the same views and colours as described in **a**. **c**, LPD-3 is coloured according to RBG domain and TM1 is coloured white. Spigot is hidden for clarity. The numbers corresponding to each RBG domain are shown at the bottom. **d**, Top-down view of LPD-3, highlighting the spiralling RBG architecture. Only the β-taco of each RBG domain is shown and the RBG domains are coloured as in **c**. **e**, Cartoon representation of RBG-5, showing the composition of tunnel-lining residues. Hydrophobic residues are coloured grey, positively charged residues are coloured blue and negatively charged residues are coloured red. Each element of the RBG architecture is labelled. **f**, Schematic of LPD-3 and Spigot. TM, transmembrane domain; H, helix. The dashed lines indicate regions of the protein that were not visible in the cryo-EM map.

Lipid organization within the tunnel

The LPD-3 model includes 7 out of its 16 RBG domains[1], which are stacked in tandem to form the rod-shaped hydrophobic tunnel that extends into the cytosol from the N-terminal transmembrane helix. Each modelled RBG domain consists of 4–5 anti-parallel β-strands that are arranged in a β-taco fold, followed by a loop-cap structure that is comprised of extended coil regions with one or more α-helices (Fig. 1c). The loop-cap covers the β-taco groove and links adjacent RBG domains. The length of the loop-cap ranges from 36 residues in RBG-3 to 64 residues in RBG-5. Multiple RBG domains also have long segments between β-strands, the longest of which is a 226-residue segment in RBG-6 that meanders along the outer surface of the β-taco, associating mainly through hydrophobic interactions. The width of tunnel gradually increases from around 25 Å in RBG-1 to approximately 40 Å in RBG-7 (roughly the tunnel midpoint), due to a combination of flattening of the β-taco and lengthening of the RBG β-strands. The sequential RBG domains form a regular, spiralling pattern involving a rotation of around 38° per domain (Fig. 1d). RBG-1

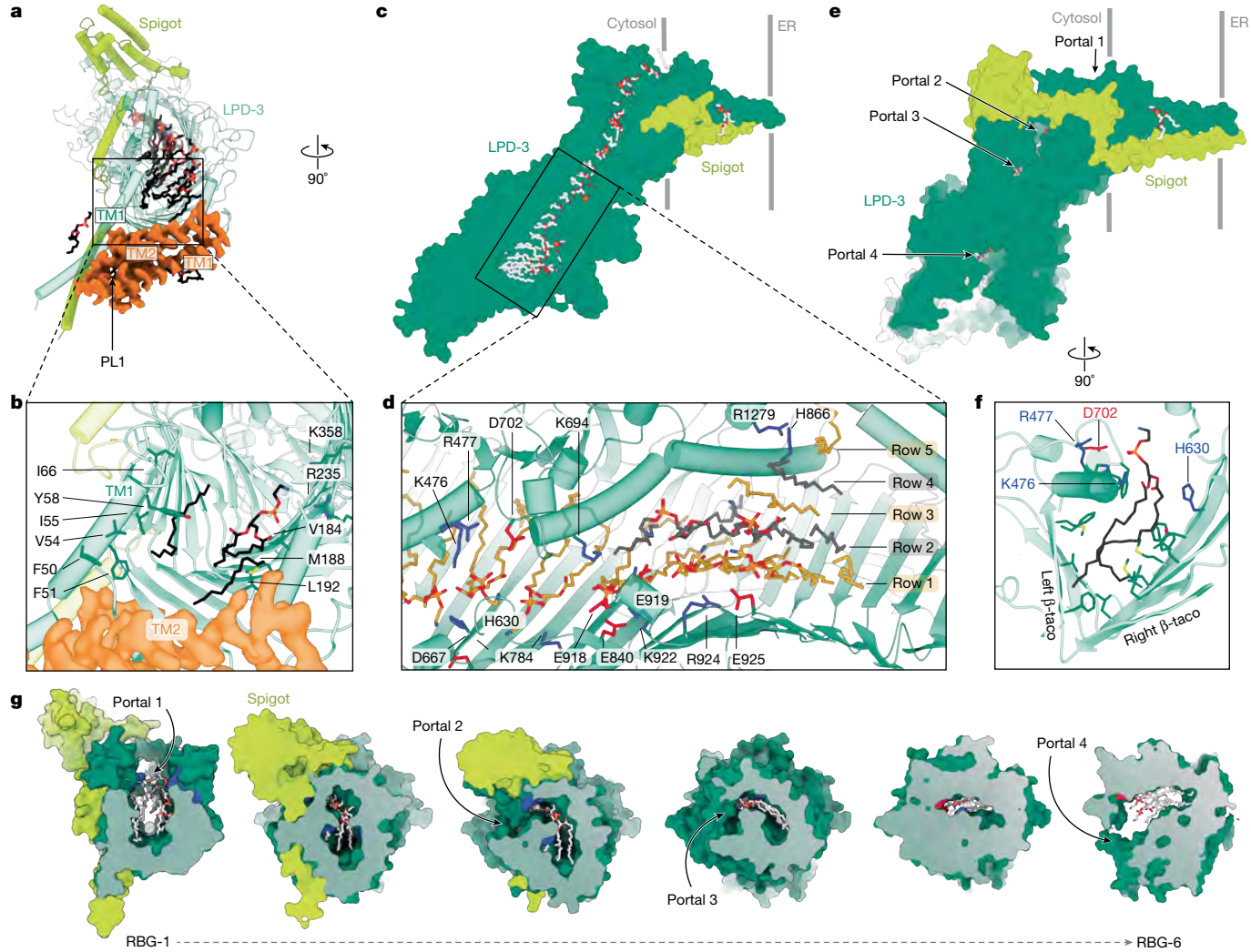

Fig. 2 | Organization of lipids in the LPD-3 tunnel. a, Overview of the lipids observed in the LPD-3 complex, shown perpendicular to the membrane. Proteins are shown as a cartoon representation and the uninterpreted cryo-EM density is shown in orange. LPD-3 is coloured teal, Spigot is coloured yellow and lipids are shown as black sticks. **b**, Magnified view of the tunnel entrance, coloured as in **a**. **c**, Clipped view to show the lipid-transport tunnel. LPD-3 and Spigot are shown as a surface representation, coloured as in **a**, and lipids are shown as white sticks. **d**, The organization of lipids within the tunnel. Ionizable residues that interact with lipid head groups are labelled and shown as sticks. Lipids are shown as grey or gold sticks. **e**, The LPD-3 complex viewed parallel to the membrane. The arrows indicate the location of the four hydration portals. Modelled proteins are shown as a surface representation and are coloured as in **a**. **f**, Magnified view of a lipid within the tunnel. Residues that interact with the lipid headgroup are shown as sticks. **g**, Sliced views of the LPD-3 tunnel, showing the locations of the hydration portals. Slices are sequential from left to right and progress from RBG-1 to RBG-6.

and RBG-7 are therefore offset by nearly 270°. As RBG domains are a defining feature of the BLTP superfamily, our structure provides a valuable experimental view of this unique architecture and demonstrates that the tunnel varies in width from entrance to midpoint.

The amino acid composition of the tunnel interior creates an environment that is ideal for solubilization and transport of membrane phospholipids. Hydrophobic residues line the β-groove and the interior-facing surfaces of the loop-caps (Fig. 1e). Moreover, a striking string of ionizable residues form a track that extends along the right edge of the β-taco and the bottom of the loop-cap (Fig. 1e). This track runs the full length of the tunnel from the membrane to RBG-7 (Extended Data Fig. 8). These largely alternating acidic and basic residues are well positioned to coordinate the head groups of the phospholipids and facilitate their transport through the tunnel.

We observed 30 density features modelled as full and partial lipid molecules that co-purified with the native LPD-3 complex; 27 are located within the tunnel and the remaining three are within the transmembrane domain (Fig. 2). As the resolution of the lipid densities was insufficient to determine their precise identity, all full lipid densities were modelled as phosphoethanolamine, consistent with the expectation that LPD-3 transports phospholipids from the ER to PM[13]. Of the three phospholipid molecules that decorate the transmembrane helices, one of which, PL1, is buried in a cavity formed by three transmembrane helices and appears to have a structural role (Fig. 2a). The entrance to the tunnel is bordered by LPD-3 TM1 and TM2 of the uninterpreted density, which form a V-shaped track with the opening of the V at the tunnel entrance (Fig. 2a,b). One partial lipid is modelled at the tunnel entrance (Fig. 2b), and a single continuous row of phospholipids lined up edge to edge spans the full length of the tunnel (Fig. 2c and Extended Data Fig. 5g). Some parts of the tunnel are larger and accommodate additional rows of lipids that are stacked up to five deep (Fig. 2d). The lipid orientations are such that all of the headgroups are near the ionizable residues along the right edges of the β-taco folds and the acyl tails extend towards the opposing edge (Fig. 2f). A similar orientation was seen for the single ordered phospholipid observed in the crystal structure of the Atg2 N-terminal RBG domain[10].

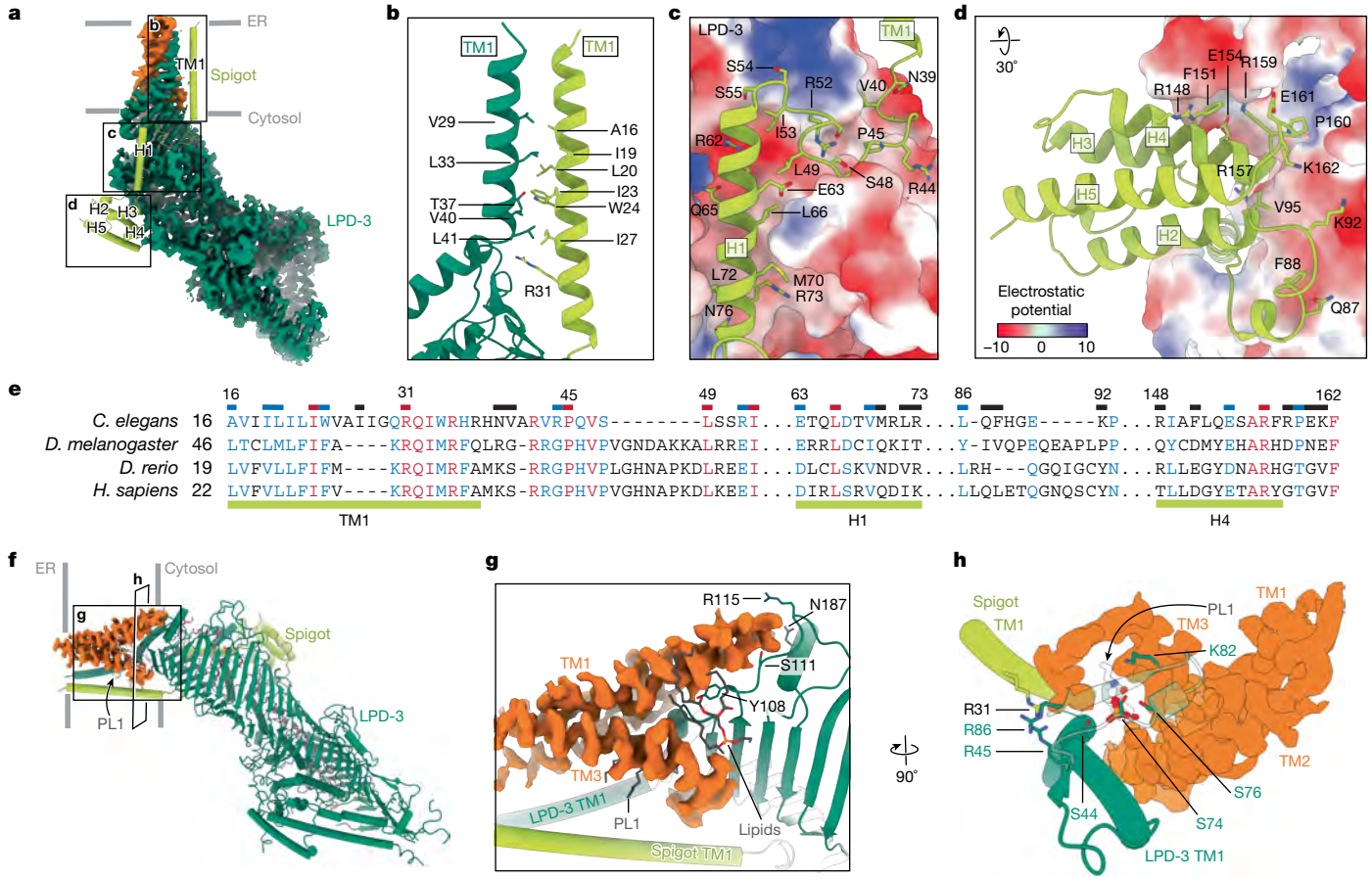

Fig. 3 | Auxiliary protein interactions with LPD-3. a, The binding interface between Spigot and LPD-3. A cryo-EM map is shown for LPD-3, coloured teal, and the uninterpreted three-helix bundle, coloured orange. Spigot is shown as a yellow cartoon. **b**, The interface between LPD-3 TM1 and Spigot TM1. The interacting residues are shown as sticks. **c**,**d**, The interface between LPD-3 and Spigot H1 (**c**) and LPD-3 and Spigot H2–H5 (**d**). The electrostatic surface of LPD-3 is shown; blue represents positive regions and red represents negative regions. Spigot is shown in yellow. **e**, Multiple-sequence alignment of Spigot orthologues. Elements of secondary structure are shown below the sequences and residues that interact with LPD-3 are indicated above with horizontal bars. Residues in black are not conserved, those in blue are conservatively substituted and those in red are conserved, as assessed using PROMALS3D[34]. *D. rerio*, *Danio rerio*; *H. sapiens*, *Homo sapiens*. **f**, The LPD-3 complex viewed parallel to the membrane. The uninterpreted three-helix bundle is shown as orange cryo-EM density. LPD-3 and Spigot are shown as a cartoon representation and are coloured teal and yellow, respectively. **g**, Putative interaction sites of the uninterpreted three-helix bundle with LPD-3. Lipid molecules are shown as black sticks and the interacting residues are shown as sticks. **h**, The LPD-3 complex viewed perpendicular to the membrane. The interacting residues are shown as sticks and phospholipid PL1 is coloured white.

Unexpectedly, the LPD-3 tunnel is punctuated by four openings that expose the interior to the aqueous cytosol (Fig. 2e). These 'hydration portals' are located in the loop-caps along the right side of the β-taco, in line with the charged residues that form the ionizable track. The portals, which range in width from 6 to 8 Å at their narrowest point, are ideally positioned to enable water molecules to access the head groups of the phospholipids (Fig. 2g), potentially facilitating lipid diffusion through the tunnel.

The number of stacked rows in various parts of the tunnel depends on the tunnel diameter. In RBG-1 and RBG-2, the tunnel diameter is sufficient to accommodate two rows of lipids. The tunnel narrows in RBG-3 and RBG-4 to fit a single row of lipids and then gradually expands through RBG-5 and RBG-6 to hold 2 to 5 rows. The increase in tunnel width and lipid rows is accompanied by an increase in the number of ionizable residues (Extended Data Fig. 8). While only 7 ionizable residues line the interior of RBG-1 and RBG-2, 11 such residues are observed in RBG-5 and RBG-6, presumably to coordinate a larger number of lipid headgroups. The interior of RBG-7 has room for lipids but no density to guide their modelling. There is an average of 4.5 lipid molecules per RBG domain within the tunnel, which means that the full-length LPD-3 molecule with 16 RBG domains can accommodate an estimated 72 lipids. Consistent with this estimation, molecular modelling of the yeast BLTP1 homologue Csf1, which contains 11 RBG domains, indicates that it can harbour 53 lipid molecules[26]. Moreover, the packing density of the lipids within the tunnel is 8.4 Å, which is consistent with the average distance between lipids in reconstituted lipid bilayers[27].

Auxiliary protein interactions with LPD-3

Two separate density features that must represent LPD-3 auxiliary proteins were observed in the N-terminal map; one was unambiguously assigned to Spigot and the other, which forms a three-helix transmembrane bundle, remains uninterpreted (Fig. 3). Spigot makes extensive contacts with LPD-3, starting in the membrane and wrapping along the tunnel exterior, burying around 3,600 Å^2 of the LPD-3 surface (Fig. 3a–d). The Spigot TM1 engages with LPD-3 TM1 through hydrophobic interactions, as well as through a hydrogen bond between Spigot Arg31, which is highly conserved (Fig. 3e), and the LPD-3 Leu41 backbone carbonyl oxygen (Fig. 3b). A linker domain that includes H1 connects Spigot TM1 to a four-helix bundle. A mixture of electrostatic and hydrophobic interactions anchor the linker domain to the outer surface of LPD-3 RBG-1 and RBG-2 (Fig. 3c). The four-helix bundle is perched on the cytosolic surfaces of both RBG-3 and RBG-4, where

the tunnel opening ends and the narrowest part of the tunnel begins. The bundle is oriented nearly perpendicular to the LPD-3 tunnel. The bundle docks into a cleft formed by a protruding loop from the RBG-4 β-taco fold, making multiple electrostatic and hydrophobic interactions (Fig. 3d). The Spigot residues that interact with LPD-3 tend to be well conserved (Fig. 3e), implying that Spigot is a conserved subunit of functional LPD-3 complexes.

The second density feature that we attribute to one or two auxiliary proteins is located exclusively within the transmembrane domain of the LPD-3 complex and is shaped like a bundle of three α-helices. This density feature could not be unambiguously assigned to any of the proteins that were identified by MS, including LTAP2 (Extended Data Fig. 3a). Although the C terminus of LTAP2 is predicted to fold into three α-helices that resemble the shape of the density feature (Extended Data Fig. 7c), we did not model LTAP2 in this location because LTAP2 is predicted to be a soluble protein, as assessed by TM-prediction software packages such as deepTMHMM[28]. Furthermore, as we did not obtain a high-resolution reconstruction of the C terminus of the LPD-3 complex, we cannot rule out the possibility that LTAP2 associates with the C-terminal region. The identity of the three-helix bundle and the location of LTAP2 in the cryo-EM structure therefore remain open questions.

Nevertheless, we note several interesting structural features of the uninterpreted density feature and its interaction with the Spigot and LPD-3 subunits. The shape and connectivity of the three α-helices suggest they correspond to the transmembrane domains of one or two auxiliary proteins (Fig. 3f). TM1 and TM2 of the density feature are connected by a cytosolic loop that contacts residues on the exterior of LPD-3 RBG-1 (Fig. 3g). TM1 and TM2 are arranged approximately parallel with LPD-3 TM1 at the tunnel entrance, positions that would allow them to have a role in lipid transfer from the membrane environment into the hydrophobic interior of the tunnel. TM3 is positioned at an approximately 45° angle relative to the other two helices (Fig. 3f) and, due to the low resolution of the density that connects TM3 to the other helices, it is possible that TM3 belongs to a separate auxiliary protein. Notably, the density at the cytosolic end of TM3 wraps beneath the LPD-3 tunnel and terminates in a buried pocket near a cluster of arginine residues, implying that this density corresponds to a C-terminal carboxylate. The buried phospholipid molecule PL1 that appears to have a structural role is enclosed in a cavity formed by transmembrane helices from LPD-3, Spigot and the uninterpreted density (Fig. 3h).

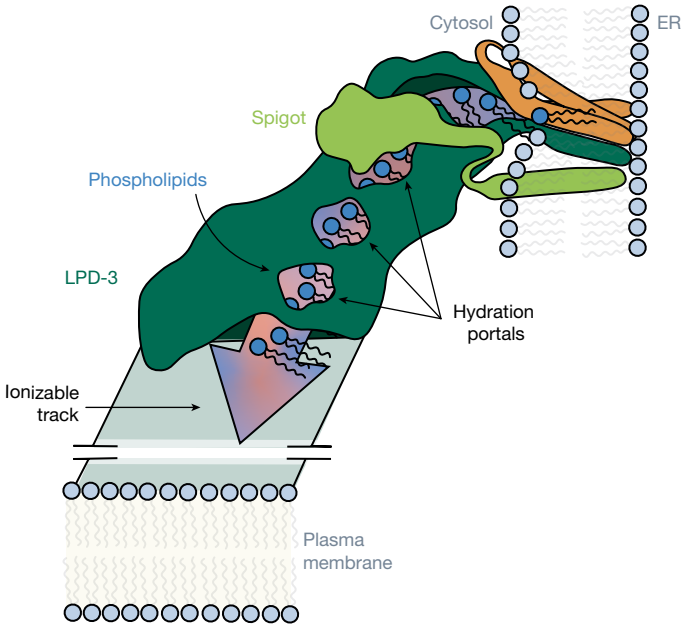

Fig. 4 | The molecular architecture of LPD-3 and putative lipid-transfer features. Cartoon representation of the LPD-3 complex, viewed parallel to the membrane, showing features of the complex that are proposed to be involved in lipid transfer. The red and blue tie-dye arrow shows the ionizable track that begins at the tunnel entrance near the ER membrane and continues through the LPD-3 tunnel, potentially to the PM. Phospholipids, depicted with blue head groups, are organized along the ionizable track. Hydration portals enable water molecules from the cytosol to access and hydrate phospholipid head groups. The uninterpreted three-helix bundle observed in the cryo-EM map is shown in orange.

Exploring the roles of Spigot and LTAP2

As MS results unambiguously identified Spigot and LTAP2 as subunits of the LPD-3 complex, we sought to investigate their role in LPD-3-mediated lipid transfer by performing RNAi-mediated knockdown in multiple model organisms. In *C. elegans*, mutation and RNAi knockdown of *lpd-3* results in reduced actin abundance and apical localization in the intestine, which could be due to the role of LPD-3 in promoting normal PM phospholipid distribution[13]. We used RNAi to knock down *spgt-1*, *LTAP2* and *lpd-3* in a *C. elegans* filamentous actin reporter strain, *act-5*::GFP[29], and we observed a 91.6% decrease in actin apical fluorescence in *lpd-3*-knockdown worms and a 79.1% decrease in *spgt-1*-knockdown worms (Extended Data Fig. 9a). These results are consistent with our RNAi-mediated knockdown experiments in *Drosophila*, which showed that knockdown of Spigot in astrocytes results in impaired clearance of neuronal debris (Extended Data Fig. 3).

Unexpectedly, we did not observe a change in actin fluorescence in *LTAP2*-knockdown *C. elegans*. Thus, to probe the function of LTAP2 further, we generated a *C. elegans* strain in which the *LTAP2* gene is knocked out (*ΔLTAP2*). We measured the developmental rate and cold tolerance of the *ΔLTAP2* worms and found that the knockout worms developed around 25% more slowly compared with WT worms (Extended Data Fig. 9b), suggesting impaired function, but we did not observe a statistically significant change in the cold survival rate compared with in the WT worms (Extended Data Fig. 9c,d). It is possible that the mild phenotype observed for loss of LTAP2 in *C. elegans* is reflective of a regulatory role for LTAP2 or is the result of the compensatory action of other proteins. By contrast, knockdown of the *Drosophila* orthologue of LTAP2 in astrocytes results in impaired clearance of neuronal debris (Extended Data Fig. 3a), mirroring the knockdown phenotype of Spigot and LPD-3 orthologues. While these results are consistent with LTAP2's being a conserved subunit in BLTP1-mediated lipid transfer, they are not conclusive, and further experiments are needed to resolve this question.

As knockdown of Spigot in *C. elegans* and *Drosophila* is a phenocopy of LPD-3 knockdown, we explored the role of C1orf43, the human orthologue of Spigot, in ER–PM contact site formation in human cells (Extended Data Fig. 9e–h). We used small interfering RNA (siRNA) to independently knock down endogenously expressed *C1orf43* and *BLTP1* in HeLa cells that were co-transfected with *GFP::MAPPER*, a GFP reporter that selectively labels ER–PM contact sites[30]. Knockdown of either protein resulted in a loss of ER–PM junctions (Extended Data Fig. 9e), indicating that C1orf43 and BLTP1 are both important for proper ER–PM contact-site formation or stability. The *Drosophila* BLTP1 orthologue Tweek is similarly required for proper formation of ER–PM contact sites[17]. We next examined the localization of recombinant C1orf43 in HeLa cells by co-transfecting the cells with plasmids encoding *C1orf43::Flag* and *GFP::MAPPER*. Notably, many of the co-transfected cells exhibited reduced viability and the surviving cells exhibited mislocalization of *GFP::MAPPER*, a possible indicator of cellular stress. Nevertheless, we observed robust localization of C1orf43 at ER–PM junctions in surviving cells (Extended Data Fig. 9g,h). These results,

together with our data showing that Spigot knockdown in *C. elegans* and *Drosophila* mirrors LPD-3-knockdown phenotypes, are consistent with a conserved role for Spigot in BLTP1-mediated lipid transfer functions at ER–PM contact sites.

Mechanistic insights into lipid transfer

Accumulating evidence from in vivo and in vitro studies indicate that BLTPs function as molecular bridges for lipid transport at ER–membrane contact sites. Our study reveals the subunit identity and architecture of the native LPD-3 complex, as well as key protein–lipid interactions that illuminate the organization and flow of lipids along the tunnel interior.

Two main auxiliary proteins were identified by MS of the LPD-3 complex, Spigot and LTAP2. Spigot interacts extensively with the N terminus of LPD-3 and is essential for proper ER–PM contact site formation in HeLa cells (Extended Data Fig. 9e), astrocyte-mediated phagocytosis in flies (Extended Data Fig. 3) and actin organization in *C. elegans* (Extended Data Fig. 9a), suggesting that it is a conserved subunit of BLTP1 complexes. The role of Spigot in ER–PM contact formation and LPD-3-mediated lipid transfer is unclear, but we speculate that it may stabilize LPD-3 and/or aid in localizing the N terminus to the ER. For LTAP2, the results do not give insight into its location in the LPD-3 complex or its role in lipid transfer. While knockout of *LTAP2* in *C. elegans* resulted in only a mild developmental delay, knockdown of the *Drosophila* orthologue in astrocytes resulted in impaired phagocytosis akin to knockdown of the Spigot and LPD-3 orthologues. Future experiments are needed to learn more about the roles of both auxiliary proteins in BLTP1-mediated lipid transfer.

In addition to the core subunits Spigot and LTAP2, it is likely that other, transiently associated auxiliary proteins interact with the LPD-3 complex to regulate lipid transfer and promote localization of the N and C termini to the ER and PM, respectively. Through a combination of MS and RNAi screening, we identified nine proteins that are important for astrocyte-mediated phagocytosis (Extended Data Fig. 3), but further studies are needed to determine whether they are involved in LPD-3-mediated lipid transfer. It is possible that some of these proteins aid in localizing the LPD-3 C terminus to the PM, a process for which the mechanism is currently unknown. The BLTP family members Vps13 and Atg2 are expected to associate with the acceptor membrane through interaction with binding partners, although the mechanism is not entirely clear[31,32].

On the basis of insights from our cryo-EM structure, we propose a model of LPD-3-mediated bulk lipid transport (Fig. 4). Phospholipids are shuttled from the ER membrane and into the tunnel through an unknown mechanism that may involve TM2 of the uninterpreted density and TM1 of LPD-3, which both border the tunnel entrance. The lipids are then organized into stacked rows by ionizable residues that line the interior of LPD-3 on the right side of the β-taco. A series of hydration portals are interspersed with the ionizable residues that allow water molecules to enter the tunnel and hydrate the lipid head groups, facilitating lipid flow. Together, these hydration portals and alternately charged ionizable residues create a continuous track that leads from the tunnel entrance, through the tunnel interior and potentially all the way to the PM. Furthermore, the organization and hydration of phospholipids within the tunnel may facilitate lipid diffusion by mimicking the environmental conditions of a lipid bilayer; the acyl tails are enclosed in a hydrophobic environment, the head groups are exposed to the solvent and the packing density is highly similar to that of a lipid bilayer. LPD-3-mediated bulk lipid transfer therefore resembles small patches of a membrane leaflet moving through a tunnel.

Future experiments with full-length LPD-3 and its orthologues will be needed to fully elaborate the mechanism of lipid transport and identify additional elements of the process, such as lipid selectivity and integration of the tunnel end point in the acceptor membrane. Finally, as mutations in human BLTP1 have been implicated in Alkuraya–Kučinskas syndrome[11,33], our studies establish a framework for structure-based investigations of the disease.

Online content

Any methods, additional references, Nature Portfolio reporting summaries, source data, extended data, supplementary information, acknowledgements, peer review information; details of author contributions and competing interests; and statements of data and code availability are available at https://doi.org/10.1038/s41586-025-08918-y.

1. Neuman, S. D., Levine, T. P. & Bashirullah, A. A novel superfamily of bridge-like lipid transfer proteins. *Trends Cell Biol.* **32**, 962–974 (2022).
2. Casares, D., Escriba, P. V. & Rossello, C. A. Membrane lipid composition: effect on membrane and organelle structure, function and compartmentalization and therapeutic avenues. *Int. J. Mol. Sci.* **20**, 2167 (2019).
3. Blom, T., Somerharju, P. & Ikonen, E. Synthesis and biosynthetic trafficking of membrane lipids. *Cold Spring Harb. Perspect. Biol.* **3**, a004713 (2011).
4. Jackson, C. L., Walch, L. & Verbavatz, J. M. Lipids and their trafficking: an integral part of cellular organization. *Dev. Cell* **39**, 139–153 (2016).
5. Wong, L. H., Gatta, A. T. & Levine, T. P. Lipid transfer proteins: the lipid commute via shuttles, bridges and tubes. *Nat. Rev. Mol. Cell Biol.* **20**, 85–101 (2019).
6. Schauder, C. M. et al. Structure of a lipid-bound extended synaptotagmin indicates a role in lipid transfer. *Nature* **510**, 552–555 (2014).
7. Hanna, M., Guillen-Samander, A. & De Camilli, P. RBG motif bridge-like lipid transport proteins: structure, functions, and open questions. *Annu. Rev. Cell Dev. Biol.* **39**, 409–434 (2023).
8. Li, P., Lees, J. A., Lusk, C. P. & Reinisch, K. M. Cryo-EM reconstruction of a VPS13 fragment reveals a long groove to channel lipids between membranes. *J. Cell Biol.* **219**, e202001161 (2020).
9. Hanna, M. G., Suen, P. H., Wu, Y., Reinisch, K. M. & De Camilli, P. SHIP164 is a chorein motif lipid transfer protein that controls endosome–Golgi membrane traffic. *J. Cell Biol.* **221**, e202111018 (2022).
10. Osawa, T. et al. Atg2 mediates direct lipid transfer between membranes for autophagosome formation. *Nat. Struct. Mol. Biol.* **26**, 281–288 (2019).
11. Kumar, K., Bellad, A., Prasad, P., Girimaji, S. C. & Muthusamy, B. *KIAA1109* gene mutation in surviving patients with Alkuraya-Kučinskas syndrome: a review of literature. *BMC Med. Genet.* **21**, 136 (2020).
12. Toulmay, A. et al. Vps13-like proteins provide phosphatidylethanolamine for GPI anchor synthesis in the ER. *J. Cell Biol.* **221**, e202111095 (2022).
13. Wang, C. et al. A conserved megaprotein-based molecular bridge critical for lipid trafficking and cold resilience. *Nat. Commun.* **13**, 6805 (2022).
14. John Peter, A. T., Cheung, N. J. & Kornmann, B. Csf1: a putative lipid transport protein required for homeoviscous adaptation of the lipidome. *Contact* **5**, 25152564221101974 (2022).
15. Tokai, M., Kawasaki, H., Kikuchi, Y. & Ouchi, K. Cloning and characterization of the *CSF1* gene of *Saccharomyces cerevisiae*, which is required for nutrient uptake at low temperature. *J. Bacteriol.* **182**, 2865–2868 (2000).
16. Verstreken, P. et al. Tweek, an evolutionarily conserved protein, is required for synaptic vesicle recycling. *Neuron* **63**, 203–215 (2009).
17. Kang, Y. J. et al. Tweek-dependent formation of ER-PM contact sites enables astrocyte phagocytic function and remodeling of neurons. Preprint at *bioRxiv* https://doi.org/10.1101/2023.11.06.565932 (2023).
18. Kumar, N. et al. VPS13A and VPS13C are lipid transport proteins differentially localized at ER contact sites. *J. Cell Biol.* **217**, 3625–3639 (2018).
19. Clark, S., Jeong, H., Goehring, A., Kang, Y. & Gouaux, E. Large-scale growth of *C. elegans* and isolation of membrane protein complexes. *Nat. Protoc.* **18**, 2699–2716 (2023).
20. Jeng, E. E. et al. Systematic identification of host cell regulators of *Legionella pneumophila* pathogenesis using a genome-wide CRISPR screen. *Cell Host Microbe* **26**, 551–563 (2019).
21. Kumar, R., Kumari, B. & Kumar, M. Prediction of endoplasmic reticulum resident proteins using fragmented amino acid composition and support vector machine. *PeerJ* **5**, e3561 (2017).
22. Valverde, D. P. et al. ATG2 transports lipids to promote autophagosome biogenesis. *J. Cell Biol.* **218**, 1787–1798 (2019).
23. Adlakha, J., Hong, Z., Li, P. & Reinisch, K. M. Structural and biochemical insights into lipid transport by VPS13 proteins. *J. Cell Biol.* **221**, e202202030 (2022).
24. Wang, Y. et al. Structural basis for lipid transfer by the ATG2A–ATG9A complex. *Nat. Struct. Mol. Biol.* **32**, 35–47 (2025).
25. Braschi, B., Bruford, E. A., Cavanagh, A. T., Neuman, S. D. & Bashirullah, A. The bridge-like lipid transfer protein (BLTP) gene group: introducing new nomenclature based on structural homology indicating shared function. *Hum. Genom.* **16**, 66 (2022).
26. Srinivasan, S., Alvarez, D., John Peter, A. T. & Vanni, S. Unbiased MD simulations identify lipid binding sites in lipid transfer proteins. *J. Cell Biol.* **223**, e202312055 (2024).
27. Tristram-Nagle, S., Petrache, H. I. & Nagle, J. F. Structure and interactions of fully hydrated dioleoylphosphatidylcholine bilayers. *Biophys. J.* **75**, 917–925 (1998).
28. Hallgren, J. T. et al. DeepTMHMM predicts alpha and beta transmembrane proteins using deep neural networks. Preprint at *bioRxiv* https://doi.org/10.1101/2022.04.08.487609 (2022).

29. Szumowski, S. C. et al. Small GTPases promote actin coat formation on microsporidian pathogens traversing the apical membrane of *Caenorhabditis elegans* intestinal cells. *Cell Microbiol.* **18**, 30–45 (2016).
30. Chang, C. L. et al. Feedback regulation of receptor-induced Ca^{2+} signaling mediated by E-Syt1 and Nir2 at endoplasmic reticulum-plasma membrane junctions. *Cell Rep.* **5**, 813–825 (2013).
31. Bean, B. D. M. et al. Competitive organelle-specific adaptors recruit Vps13 to membrane contact sites. *J. Cell Biol.* **217**, 3593–3607 (2018).
32. Gomez-Sanchez, R. et al. Atg9 establishes Atg2-dependent contact sites between the endoplasmic reticulum and phagophores. *J. Cell Biol.* **217**, 2743–2763 (2018).
33. Gueneau, L. et al. KIAA1109 variants are associated with a severe disorder of brain development and arthrogryposis. *Am. J. Hum. Genet.* **102**, 116–132 (2018).
34. Pei, J., Tang, M. & Grishin, N. V. PROMALS3D web server for accurate multiple protein sequence and structure alignments. *Nucleic Acids Res.* **36**, W30–W34 (2008).

Methods

Transgenic *C. elegans* design

All transgenic *C. elegans* strains were generated by SunyBiotech using CRISPR–Cas9 genome engineering. To generate the *lpd3::mVenus* worm line (strain PHX5024 lpd-3 (syb5024)), the mVenus-3×Flag sequence was inserted before the stop codon of the endogenous *lpd-3* gene (Wormbase: Y47G6A.23). The genotype was confirmed using PCR with the primers ER16-seq-s (GAAAAGTACAATCCCTGCCA) and ER16-seq-a (ACTTTCTGCGTTTGCGTGTG), which bind 469 bp upstream and 318 bp downstream from the insertion site to amplify the region of interest. To generate the *mVenus::lpd3* worm line (strain PHX5131 lpd-3 (syb5131)), the 3×Flag-mVenus sequence was inserted after the start codon of the endogenous *lpd-3* gene and a signal sequence was not added before the insertion. The genotype was confirmed using PCR and primers ER15-seq-s (AAATGCACAAAACCTGTGTG) and ER15-seq-a (AAGCGATCAAAGAGGAGAAT), which bind 432 bp upstream and 388 bp downstream from the insertion site. To enable elution of the engineered LPD-3 complex from affinity chromatography resin, a PreScission protease (3C) cleavage site was placed between the mVenus fluorophore and 3×Flag tag for both worm lines. To generate the *ΔLTAP2* knockout worm line (strain PHX9850 Y38C1AA.12a(syb9850)), base pairs 32–1520 of the 1,583 bp *LTAP2* gene were deleted, resulting in a frameshift and new termination codon. The genotype was confirmed using PCR and primers SCK04-ko-s (CGAGAGAATGGGTTCAAAGG) and SCK04-ko-a (TACGCTAAACAACACGCGAC), which bind 437 bp upstream and 345 bp downstream from the insertion site.

Spectral confocal imaging

Adult and larval worms were immobilized in M9 buffer (22 mM KH_2PO_4, 42 mM Na_2HPO_4, 86 mM NaCl, and 1 mM $MgCl_2$) containing 30 mM sodium azide and placed on slides that were prepared with ~4 mm agar pads. Spectral images were acquired on the Zeiss 34-channel LSM 880 Fast Airyscan inverted microscope with a 40×/1.2 NA water-immersion objective lens. Linear unmixing was used to distinguish between the mVenus signal and autofluorescence. The autofluorescence signal was subtracted from each image. The 3D *z*-stack information is presented in 2D after performing a maximum-intensity projection. Six worms were randomly chosen for imaging. No statistical methods were used to predetermine sample size.

C. elegans development and cold-resilience assays

Developmental and cold-resilience assays were performed in accordance with protocol developed previously[13]. Worms were cultured at 20 °C on HB101-seeded nematode growth medium (NGM) for at least four generations and were never starved. To analyse the developmental rate of WT and transgenic worm lines, bleach synchronized worms were cultured at 20 °C on NGM. At 40, 45 or 50 h after plating, the percentage of worms reaching the L4 stage (determined by the presence of a crescent-shaped vulva) was counted.

To analyse the cold resilience of WT, *lpd3::mVenus* and *mVenus::lpd3* worm lines, bleach-synchronized worms were cultured for 50 h at 20 °C on NGM. At 50 h, the worms were counted and the presence of any dead worms was recorded. Immediately afterwards, the worms were placed at 4 °C for 20 h, then removed and allowed to recover at 20 °C for 24 h before the percentage of survivors was determined. Worms were considered to be dead if they appeared necrotic, displayed no pharynx pumping, and did not move in response to plate tapping when observed using light microscopy.

To analyse the cold-resilience and freeze-resilience of *ΔLTAP2* worms in comparison to WT and *mVenus::lpd3* worm lines, worms were not bleach synchronized but, rather, L4-stage worms were picked onto plates with a fresh HB101 lawn and placed at either 4 °C for 20 h or −20 °C for 45 min. The worms were then removed and allowed to recover at 20 °C for 24 h before the percentage of survivors was determined according to the same criteria as described above. Notably, we observed that worms that were not bleach synchronized before the cold-tolerance assays had a higher rate of survival compared with those that were bleach synchronized. Statistical analyses were performed using GraphPad Prism 9. For all worm development and cold resilience experiments, each plate of worms harbored an average of 20 worms, and 9–12 plates were counted per experimental group. No statistical methods were used to predetermine sample size; sample size was determined on the basis of published studies[13].

RNAi knockdown of LPD-3 complex subunits

The *lpd-3* RNAi construct was a gift from Z. Zhou and was created by inserting base pairs 3019–3572 of the *lpd-3* coding sequence into the L4440 vector. The *spgt-1* and *LTAP2* RNAi constructs were generated by inserting base pairs 22–559 of *spgt-1* and 44–527 of *LTAP2* into L4440 vectors. L4-stage *C. elegans* of the strain jyIs13 [*act-5p::GFP::act-5* + *rol-6 (su1006)*] (CGC ERT60) were transferred onto freshly prepared RNAi plates containing either empty vector control (L4440) or RNAi constructs targeting *lpd-3*, *spgt-1* or *LTAP2*. The worms were incubated on these plates for 40 h. Subsequently, 40 adult worms from each condition were transferred to newly prepared RNAi plates and allowed to lay eggs for 3 h. Next, the adults were removed, and the progeny were imaged at the adult stage using the Zeiss LSM 880 confocal microscope. On the basis of previous studies[13], worms with tight apical GFP expression were categorized as WT, while those displaying loss of GFP signal and vesicle formation were classified as having a phenotype. For each condition, 24–27 adult worms were randomly chosen for imaging. No statistical methods were used to predetermine sample size.

Large scale *C. elegans* culture

Large-scale worm growth and optimization of LPD-3 protein isolation conditions were performed as described previously[19]. In brief, NGM agar plates were prepared and spread with *E. coli* strain HB101, allowing the bacterial lawn to grow overnight at 37 °C. Worms of mixed larval and adult stages were transferred to the NGM plates and grown for 3–4 days at 20 °C until HB101 cells were depleted. Worms on the plates were transferred to a liquid medium in 2 l baffled flasks, supplemented with HB101 (~15 g per 500 ml medium) and streptomycin (50 μg ml^{-1}), and the worms were grown at 20 °C with vigorous shaking (150 rpm) for 70–72 h. To collect worms, the liquid culture flasks were placed on ice for 1 h to allow the worms to settle. The medium was removed and the worm slurry was collected in a tube, washed twice with 50 ml of ice cold M9 buffer by successive centrifugation (800*g* for 1 min) and resuspension. Worms were 'cleaned' by sucrose density centrifugation at 1,500*g* for 5 min after bringing the volume of worm slurry up to 25 ml with M9 buffer and adding 25 ml of ice cold 60% (w/v) sucrose. The worm layer on top was recovered and placed into a new tube and then washed twice with 50 ml of ice cold M9 buffer. The volume of the worm pellet was measured and the same volume of M9 buffer was added to the tube and worm balls were made by dripping the slurry into liquid nitrogen. The worm balls were stored at −80 °C until further use.

Isolation of the native LPD-3 complex

Approximately 40 g of frozen worm balls was disrupted using a ball mill (MM400, Retch); the grinding jar and ball were pre-cooled in liquid nitrogen. Disrupted worm powder was solubilized at 4 °C for 2.5 h in a buffer containing 50 mM Tris-Cl (pH 8), 150 mM NaCl, 5 mM EDTA, 2% (w/v) glyco-diosgenin (GDN) and protease inhibitors (0.8 μM aprotinin, 2 μg ml^{-1} leupeptin and 2 μM pepstatin). After centrifugation at 40,000 rpm (186,000*g*) for 50 min, the supernatant was filtered through a 0.45 μm filter and incubated with anti-Flag M2 affinity gel for 2.5 h on a rotator at 4 °C. The resin was washed five times with a buffer containing 20 mM Tris-Cl (pH 8), 150 mM NaCl and 0.02% (w/v) GDN, using a volume of buffer that was 200-fold the volume of the resin. The LPD-3 complex was eluted by incubating with 10 μg of 3C protease

at 4 °C for 1 h on the rotator. The sample was concentrated to 100 µl using a 100 kDa MWCO concentrator and the concentrate was loaded onto a SEC column (Superose 6 Increase 10/30 GL, GE Healthcare), equilibrated in a buffer composed of 20 mM Tris-Cl (pH 8), 150 mM NaCl and 0.02% (w/v) GDN. The peak fractions from the putative LPD-3 complex were pooled and concentrated for cryo-EM grid preparation or MS experiments. Approximately 250 ng of LPD-3 was isolated from 40 g of worm balls, which are equal to 3×10^7 worms. The amount of protein was determined through mVenus fluorescence on the basis of comparison to an mVenus standard curve on the FSEC. The isolated native LPD-3 sample was analysed by SDS–PAGE and the protein bands were visualized by silver staining.

The same isolation method was used to make the WT worm sample from the *C. elegans* N2 strain for use as a control in the MS experiments. Approximately 40 g of N2 worm balls was purified using anti-Flag M2 resin, followed by purification on an SEC column, and the fractions in the same elution volume as LPD-3 were collected, pooled and concentrated. The concentrate was subjected to MS analysis to evaluate non-specific binding of *C. elegans* proteins to anti-Flag M2 affinity resin.

MS

The SEC-purified LPD-3 complex sample was dried and then dissolved in a solution consisting of 5% SDS, 8 M urea and 100 mM glycine (pH 7.55). The sample was then reduced with tris(2-carboxyethyl)phosphine at 37 °C for 15 min and alkylated with methyl methanethiosulfonate for 15 min at room temperature, followed by addition of acidified 90% methanol and 100 mM triethylammonium bicarbonate buffer (TEAB; pH 7.55). The sample was then digested in an S-trap micro column briefly with 2 µg of a Tryp/LysC protease mixture, followed by a wash and 2 h digestion at 47 °C with trypsin. The peptides were eluted with a solution consisting of 50 mM TEAB, 50% acetonitrile and 0.2% formic acid, and were then pooled and dried. Each sample was dissolved in 20 µl of 5% formic acid and injected into the Thermo Fisher QExactive HF mass spectrometer. Protein digests were separated using a Dionex RSLC UHPLC system, then delivered to a QExactive HF (Thermo Fisher) by electrospray ionization using a Nano Flex Ion Spray Source (Thermo Fisher Scientific) that is fitted with a 20-µm stainless-steel nano-bore emitter spray tip and a 2.6 kV source voltage. Xcalibur v.4.0 was used to control the system. The samples were applied at 10 µl min^{-1} to a Symmetry C18 trap cartridge (Waters) for 10 min, then switched onto a 75 µm × 250 mm NanoAcquity BEH130 C18 column with 1.7 µm particles (Waters) using mobile phases water (A) and acetonitrile (B) containing 0.1% formic acid and a 7.5 to 30% acetonitrile gradient over 60 min with a 300 nl min^{-1} flow rate. Survey mass spectra were acquired over m/z 375 to 1,400 at 120,000 resolution (m/z 200), and data-dependent acquisition selected the top-ten most abundant precursor ions for tandem MS by higher energy collisional dissociation using an isolation width of 1.2 m/z, normalized collision energy of 30 and a resolution of 30,000. Dynamic exclusion was set to auto, charge state for MS/MS +2 to +7, maximum ion time 100 ms, minimum AGC target of 3×10^6 in MS1 mode, and 5×10^3 in MS2 mode. Data analysis was performed using Comet (v.2016.01, rev. 3)[35] against a January 2022 version of canonical FASTA protein database containing *C. elegans* UniProt sequences and concatenated sequence-reversed entries to estimate error thresholds and 179 common contaminant sequences and their reversed forms. Comet searches for all samples were performed with trypsin enzyme specificity. Monoisotopic parent ion mass tolerance was set to 1.25 Da and monoisotopic fragment ion mass tolerance was set to 1.0005 Da. A static modification of +45.9877 Da was added to all cysteine residues and a variable modification of +15.9949 Da on methionine residues. A linear discriminant transformation was used to improve the identification sensitivity from the Comet analysis[36,37]. Separate histograms were created for matches to forward sequences and for matches to reversed sequences for all peptides of seven amino acids or longer. The score histograms of reversed matches were used to estimate peptide false-discovery rates (FDRs) and set score thresholds for each peptide class. The overall protein FDR was 1.2%.

Drosophila RNAi screen

Flies (*D. melanogaster*) were reared on standard cornmeal agar under a 12 h–12 h light–dark cycle at 25 °C. All of the experimental procedures were carried out at 25 °C. Auxiliary binding partners of LPD-3 were screened, focusing on proteins unrelated to transcription, translation, protein folding or the cytoskeleton. *Drosophila* homologues of these selected proteins were subjected to RNAi-mediated knockdown in astrocytes using the *GMR25H07-Gal4* driver line (Bloomington, 49145). For each RNAi condition, five flies were dissected at head eversion, a developmental stage occurring approximately 12 h into metamorphosis, characterized by the emergence of the immature adult head. Flies were selected randomly for treatment and both males and females were used for experiments. Researchers were blinded regarding the target gene of each RNAi. No statistical methods were used to predetermine sample size.

The following lines were used: *UAS-FLP5.DD*, *UAS-tweek* RNAi (VDRC, 110686), *CG6665* RNAi (Bloomington, 60402), *CG10874* RNAi (NIG-Fly, 10874R-3), *Pepck2* RNAi (VDRC, 107092), *Apoltp* RNAi (Bloomington, 51937), *CG33303* RNAi (VDRC, 107778), *FASN1* RNAi (VDRC, 108339), *SERCA* RNAi (VDRC, 107446), *SdhA* RNAi (VDRC, 110440), *Rack1* RNAi (VDRC, 104470), *PCB* RNAi (VDRC, 105936), *Rab1* RNAi (Bloomington, 27299) and *Idh* RNAi (VDRC, 100554).

For sample collection, prepupae were placed onto a 1% agarose plate, and the dissection of the central nervous system (CNS) was conducted every 10 min at head eversion. Dissected samples were initially placed in PBS with 0.1% Triton X-100 (0.1% PBST) on ice and then transferred to a solution containing 4% formaldehyde in PBST for fixation, which lasted for 20 min at room temperature with gentle agitation. After fixation, the samples underwent two washes in 0.1% PBST and were subsequently incubated with primary antibodies in 0.1% PBST on a shaker at 4 °C overnight. Washes were conducted in 0.1% PBST at room temperature for 5 min each, followed by overnight incubation at 4 °C on a shaker in 0.1% PBST. Next, the samples were exposed to secondary antibody in 0.1% PBST for 3 h at room temperature, followed by additional washing and storage in 0.1% PBST overnight at 4 °C. Finally, the samples were mounted using Vectashield antifade reagent. The primary antibody used for larvae staining was anti-Crz (Crz, 1:1,000), and the secondary antibody used was Cy3 (Jackson ImmunoResearch, 1:500). Fixed fly CNS samples were imaged using a Zeiss LSM 880 confocal microscope. Image tiles were stitched together. The area of vCrz (ventral nerve cord expressing Corazonin) neurites (without cell bodies) was quantified and statistics were performed using GraphPad Prism 9.

Anti-Crz antibody production and validation

A custom polyclonal antibody against *D. melanogaster* Corazonin (Crz) was generated in rabbits (Genemed Synthesis). Rabbits were immunized with a KLH-conjugated synthetic peptide (VDPDPENSAHP RLSN) corresponding to amino acids 97–111 of the Crz protein (UniProt: Q26377). Antiserum was affinity-purified against the immunizing peptide. Antibody specificity was confirmed by co-localization with *Crz-Gal4*-driven *UAS-mCD8-GFP* expression in *Drosophila* larval ventral nerve cords.

Cell culture

HeLa cells were maintained at 37 °C in Dulbecco's modified Eagle medium (DMEM) (Gibco) with 10% FBS and 4 mM glutamine (complete medium). Cells were cultured on chambered cover glass (18 mm diameter, #11/2 thickness cover glass, Electron Microscopy Sciences). Cells that were transfected with a plasmid alone were transfected with GFP-Mapper (Addgene, 117721) or C1ORF43-FLAG (SinoBiologic) constructs using lipofectamine 3000 (Invitrogen), according to the manufacturer's instructions. Cells were transfected at the 100 ng–200 ng

range. Cells were fixed and imaged 48 h after transfection. Cells that were transfected with plasmid and siRNA were transfected with DharmaFECT Duo Transfection Reagent according to the manufacturer's instructions. SMARTPools of siRNA were used for *KIAA1109* (*BLTP1*) and *C1orf43*. Cells were fixed and imaged 48 h after transfection of siRNA.

All experiments were performed in 12-well cell culture plates (TrueLine) and, once the cells were transfected, they were maintained in Opti-MEM reduced-serum medium (Gibco). Cells were fixed in 0.1% Triton X-100 (0.1% PBST) with 1% formaldehyde for 30 min, washed, put in blocking buffer (1% BSA in PBS) for 30 min and then washed again. Primary antibody stains were done overnight at 4 °C on a shaker. Primary antibodies were then removed, and the samples were washed three times with PBS. Secondary antibodies were applied for 1 h at room temperature while shaking. The samples were washed with PBS and mounted onto slides with Prolong Gold antifade (Invitrogen). The primary antibodies used for cell culture stain were as follows: anti-GFP (Abcam, 1:1,000) and anti-Flag (Sigma-Aldrich 1:250).

The samples were imaged using the Zeiss LSM 880 confocal microscope with Airyscan Fast mode. For colocalization analysis, a 100 μm^2 region of cells was used to calculate the percentage of C1orf43–Flag expression in *GFP::MAPPER*. For control images, each *GFP::MAPPER* image was horizontally flipped and colocalization was calculated. HeLa cells were obtained from the ATCC and were not authenticated. The cells were tested negative for mycoplasma contamination. Statistical analyses were performed using GraphPad Prism 9.

Cryo-EM sample preparation

A volume of 3.5 µl of the concentrated LPD-3 complex was applied to a Quantifoil grid (R2/1 300 gold mesh, covered by 2 nm continuous carbon film), which was glow-discharged at 15 mA for 30 s in the presence of amylamine. The grids were blotted and flash-frozen using the Vitrobot mark IV for 2.5 s with 0 blot force after 10 s wait time under 100% humidity at 10 °C. The grids were plunge-frozen into liquid ethane, cooled by liquid nitrogen.

Data acquisition

The native LPD-3 complex dataset was collected on the 300 keV FEI Titan Krios microscope equipped with a K3 detector. The micrographs were acquired in super-resolution mode (0.394 Å px^{-1}) with a magnification of ×29,000 corresponding to a physical pixel size of 0.788 Å px^{-1}. Images were collected by a 3 × 3 multi-hole per stage shift and a 7 multi-shot per hole method using Serial EM, with a defocus range of −1.5 to −2.5 µm. Each video stack consisted of 50 frames per video, with a total dose of 50 $e^- Å^{-2}$. A total of 8,195 videos was collected.

Image processing

Beam-induced motion was corrected by patch motion correction with an output Fourier cropping factor of 1/2 (0.788 Å px^{-1}). Contrast transfer function (CTF) parameters were estimated by patch CTF estimation in CryoSparc v.3.3.1. A total of 8,061 videos was selected by manual curation and the particles were picked using blob-picker with an elliptical blob in which the minimum and maximum particle diameters were set to 100 and 400 Å, respectively. Initially, 3.9 million particles were picked and, after particle inspection, 2.6 million particles were extracted with a box size of 756 pixels, 4× binned (3.152 Å px^{-1}). After three rounds of 2D classification, 'junk' particles were removed, resulting in 938,732 million particles in total. The classes with the highest-resolution features were selected to generate an ab initio model. All 938,732 particles were then subjected to one round of heterogenous refinement using the ab initio model as a reference to further remove junk particles. The best class contained 861,293 particles that were re-extracted from unbinned micrographs and subjected to one more round of heterogeneous refinement. Two classes, containing 713,216 particles total, were selected for non-uniform refinement and the resulting map was used to generate templates for template picking. Approximately 2.1 million particles were extracted from unbinned micrographs with a box size of 756 pixels and subjected to two rounds of 2D classification and one round of heterogeneous refinement. The best class, which contained 285,377 particles, was selected for non-uniform refinement, yielding a 2.7-Å reconstruction of the N-terminal half of LPD-3.

We note that many of our 2D classes contained features that are consistent with a full-length protein. We selected the classes with the strongest full-length features and re-extracted them with a box size of 1,024, 2× binned (1.576 Å px^{-1}). All 146,403 particles were used to generate an ab initio model, which was then subjected to non-uniform refinement. As the refined volume was centred near the N terminus, we used the volume alignment tool in CryoSparc to recentre the volume on the middle of the protein. Non-uniform refinement of the shifted volume resulted in a nominal 6.2 Å reconstruction of the full-length LPD-3 complex.

Atomic model building and refinement

The N-terminal density map was sharpened using Phenix AutoSharpen, and both sharpened and unsharpened maps were used for structure determination. The initial model of LPD-3, residues 1–1950, was predicted by AlphaFold2 (ref. 38) and fit into the map with rigid body fitting in UCSF ChimeraX[39], followed by manual adjustment and de novo model building in Coot (v.0.9.8.92)[40]. De novo regions were built by tracing the backbone, assigning the sequence and fitting the side chains using Coot. The model was refined with the real space refinement program in PHENIX (v.1.21)[41]. Although there is density corresponding to one more RBG domain (RBG-8) in the map, the domain was not modelled due to low resolution. The following regions of LPD-3 were not modelled due to lack of density: 1–20, 164–180, 1115–1146, 1209–1231, 1299–1301, 1327–1339, 1355–1380, 1400–1420 and 1680–4022.

The structure of the Spigot auxiliary protein was built using a combination of de novo model building and rigid-body fitting of the AlphaFold2-predicted structure. Each α-helix was individually docked into the map and manually adjusted in Coot, using the side chains of bulky tryptophan, tyrosine and phenylalanine residues, including Trp24, Tyr94, Phe151 and Phe163, as guides to correctly assign register. Spigot residues 1–6 and 188–276 were not modelled due to a lack of density.

The phospholipid molecules were identified on the basis of a V-shaped density feature and all phospholipids were modelled as 1,2-dioleoyl-sn-glycero-3-phosphoethanolamine. The number of carbon molecules in the acyl chain was modified on the basis of the density; the length of acyl chains ranged from C3 to C16. Partial lipid densities were built in regions where an acyl chain of ten or more carbons could be fit in the density feature.

Reporting summary

Further information on research design is available in the Nature Portfolio Reporting Summary linked to this article.

Data availability

The volumes for the cryo-EM data have been deposited at the Electron Microscopy Data Bank under accession codes EMD-45276 (full-length) and EMD-45399 (N-terminal). The coordinates of the LPD-3 complex have been deposited at the Protein Data Bank under accession code 9CAP. The full version of the silver-stain gel is included in Supplementary Fig. 1, and the sequences for all RNAi constructs are included in Supplementary Tables 1 and 2. The UniProt accession number for LPD-3 is A0A0K3AWP8. The UniProt accession number for Spigot is Q4W5H0. The UniProt accession number for LTAP2 is U4PLN7. Source data are provided with this paper.

35. Eng, J. K., Jahan, T. A. & Hoopmann, M. R. Comet: an open-source MS/MS sequence database search tool. *Proteomics* **13**, 22–24 (2013).
36. Wilmarth, P. A., Riviere, M. A. & David, L. L. Techniques for accurate protein identification in shotgun proteomic studies of human, mouse, bovine, and chicken lenses. *J. Ocul. Biol. Dis. Inform.* **2**, 223–234 (2009).

37. Keller, A., Nesvizhskii, A. I., Kolker, E. & Aebersold, R. Empirical statistical model to estimate the accuracy of peptide identifications made by MS/MS and database search. *Anal. Chem.* **74**, 5383–5392 (2002).
38. Jumper, J. et al. Highly accurate protein structure prediction with AlphaFold. *Nature* **596**, 583–589 (2021).
39. Pettersen, E. F. et al. UCSF Chimera—a visualization system for exploratory research and analysis. *J. Comput. Chem.* **25**, 1605–1612 (2004).
40. Emsley, P., Lohkamp, B., Scott, W. G. & Cowtan, K. Features and development of Coot. *Acta Crystallogr. D* **66**, 486–501 (2010).
41. Adams, P. D. et al. PHENIX: building new software for automated crystallographic structure determination. *Acta Crystallogr. D* **58**, 1948–1954 (2002).

Acknowledgements We thank P. A. Karplus for help with structure analysis and manuscript preparation; E. Gouaux and the members of the Gouaux laboratory for discussions; A. Reddy for MS analysis; F. Jalali-Yazdi for help with cryo-EM data processing; Z. Zhou for providing the *lpd-3* RNAi construct; and T. Evans for help with *C. elegans* RNAi experiments. This work was supported by Howard Hughes Medical Institute funding to E. Gouaux; Oregon State University startup funds to S.C.; US National Institutes of Health (NIH) grant K99 NS126642 to Y.K.; and NIH grants R37 NS053538-18 and R01 NS124146-01 to M.F. A portion of this research was supported by NIH grant R24GM154185 and was performed at the Pacific Northwest Center for Cryo-EM with assistance from M. Miletto. The OHSU Proteomics Shared Resource is partially supported by NIH core grants P30EY010572 and P30CA069533.

Author contributions S.C. performed the cryo-EM experiments. Y.K. and A.J. performed the RNAi screen and astrocyte-mediated phagocytosis assays in *Drosophila*. Y.K. generated the constructs for cell culture experiments and K.S.L. performed the experiments. Y.K. performed the worm RNAi experiments in *C. elegans*. M.P. provided guidance and training for *C. elegans* experiments. H.L. performed functional analyses of transgenic worm lines. Y.K., M.F. and S.C. designed the project and wrote the manuscript. All of the authors contributed to the manuscript preparation.

Competing interests The authors declare no competing interests.

Additional information
Supplementary information The online version contains supplementary material available at https://doi.org/10.1038/s41586-025-08918-y.
Correspondence and requests for materials should be addressed to Sarah Clark.
Peer review information *Nature* thanks Stefano Vanni, Osamu Nureki and the other, anonymous, reviewer(s) for their contribution to the peer review of this work. Peer reviewer reports are available.

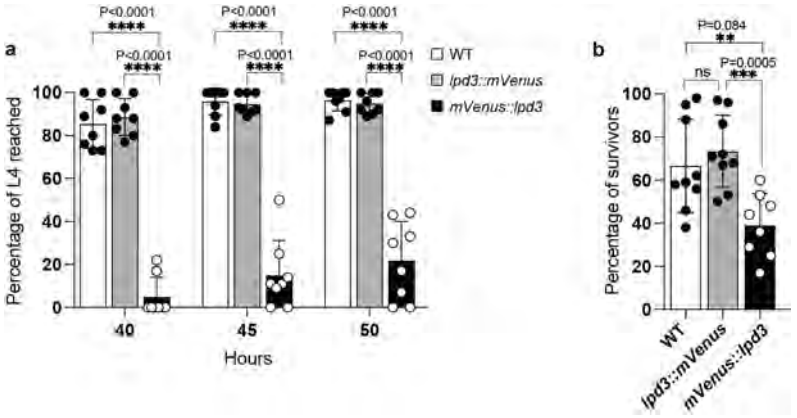

Extended Data Fig. 1 | Development and cold tolerance of wild type and transgenic worms. a, Percentages of animals that reached developmental L4 stage at indicated hours post egg preparation in wild type (WT) worms, *lpd3::mvenus* worms, or *mvenus::lpd3* worms. **b**, Percentages of animals that survived cold exposure (4 °C for 20 h) post egg preparation in wild type (WT) worms, *lpd3::mvenus* worms, or *mvenus::lpd3* worms. **P < 0.01, ***P < 0.001, ****P < 0.0001, ns=not significant. Values are means +/− S.D. (two-sided unpaired t-test, N = 9 biological replicates).

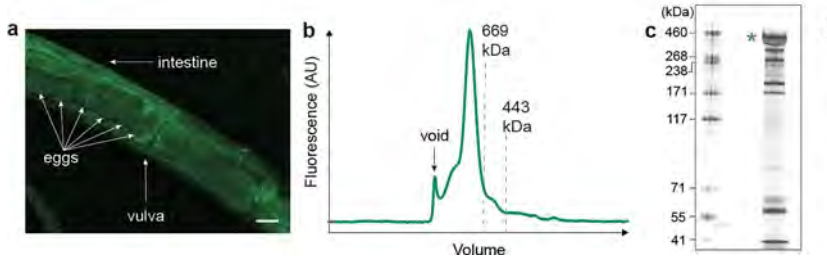

d

Name	LPD-3 pSC	Control pSC	MW (kDa)	Uniprot ID
LPD-3	2577	2	452.1	A0A0K3AWP8
LTAP2	201	0	35.2	U4PLN7
Spigot	118	0	31.5	Q4W5H0

Extended Data Fig. 2 | Isolation of LPD-3 from *C. elegans*. **a**, Spectral confocal image of mVenus fluorescence in an *lpd3::mvenus* worm showing fluorescence throughout the worm body. Shown is one representative image of six total images. **b**, Representative FSEC profile of the LPD-3 complex, detected via tryptophan fluorescence. **c**, A silver stained SDS-PAGE gel of the purified LPD-3 complex. Teal asterisk indicates LPD-3. Other bands may correspond to transiently associated proteins or contaminants. The experiment was repeated two times with similar results. For gel source data, see Supplementary Fig. 1. **d**, Mass spectrometry analysis of the purified LPD-3 complex, showing the three proteins with the highest peptide spectral counts (pSC).

a

C. elegans gene name	*D. melanogaster* gene name	*C. elegans* Uniprot ID	*D. melanogaster* Uniprot ID	Phagocytosis defect?	LPD-3 pSC	Control pSC
Lpd-3	*Tweek*	A0A0K3AWP8	X2JA38	YES	2577	2
Y38C1AA.12	*CG10874*	U4PLN7	E4NKL4	YES	201	0
Spgt-1	*CG6665*	Q4W5H0	A1ZAM0	YES	118	0
Pck-1	*Pepck2*	O44906	Q7JXB5	YES	18	0
Pck-2	*Pepck2*	O02286	Q7JXB5	YES	6	0
Vit-1	*Apoltp*	P55155	Q7KTG2	YES	16	3
Ribo-1	*CG33303*	Q9GZH4	Q76NQ0	YES	15	0
Fasn-1	*FASN1*	P91871	B7Z001	NO	15	1
Sca-1	*SERCA*	G5EEK8	P22700	YES	11	3
Sdha-1	*Sdha*	Q09508	Q94523	NO	10	0
Rack-1	*Rack1*	Q21215	O18640	YES	11	0
Pyc-1	*PCB*	O17732	Q0E9E2	YES	8	0
Rab-1	*Rab*	Q9UAQ6	O18332	YES	7	0
Ldh-1	*Ldh*	H9G2T4	B7Z0E0	YES	9	0

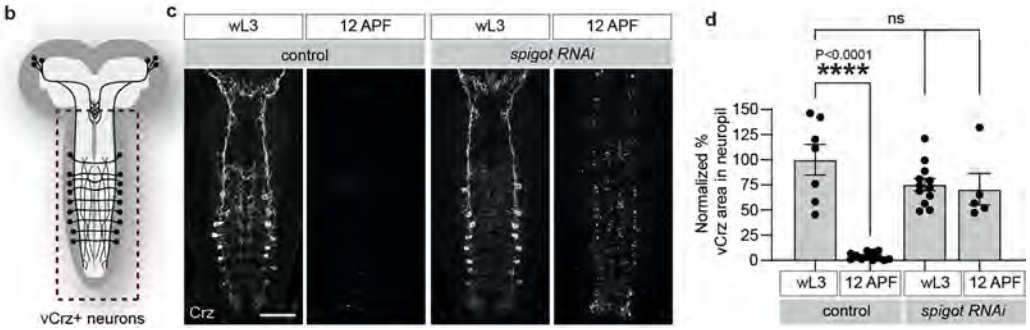

Extended Data Fig. 3 | RNAi screen in *Drosophila*. a, Mass spectrometry analysis of the LPD-3 complex, showing the proteins that were subjected to RNAi-mediated knockdown in *Drosophila* astrocytes to in order to identify regulators of phagocytosis. Y38C1AA.12 lacks a gene name in *C. elegans* and is referred to in this text as LTAP2. pSC = peptide spectral counts. For the sequences of each RNAi construct, see Supplementary Table 2. **b**, Overview of vCrz neuron morphology: Eight pairs of vCrz neurons are present in the ventral nerve cord, red dotted box represents imaged region. **c**, vCrz neuronsat the wandering third instar larval stage (wL3) in controls which is broken down and fully cleared by astrocytes at head eversion (HE, ~12 h after puparium formation) in controls. Astrocyte knockdown of *spigot* (*CG6665*) with *GMR25H07-Gal4* (astrocyte-specific driver) does not affect neuronal morphology at wL3 but disrupts the ability of astrocytes to clear neuronal debris by HE. vCrz neurons were labelled with anti-Crz, and all images are maximum Z projections of the entire ventral nerve cord (VNC). Scale bar, 50 µm. **d**, Quantification of data from (**c**) for controls (*UAS-FLP5.DD*) (wL3, N = 7; HE, N = 12) and *UAS-spigot RNAi* (wL3, N = 12; HE, N = 5). Graphs show mean ± SEM, and each dot represents independent animals. Statistical comparisons were performed using two-way ANOVA with Sidak's multiple comparisons test. ****P < 0.0001, ns=not significant.

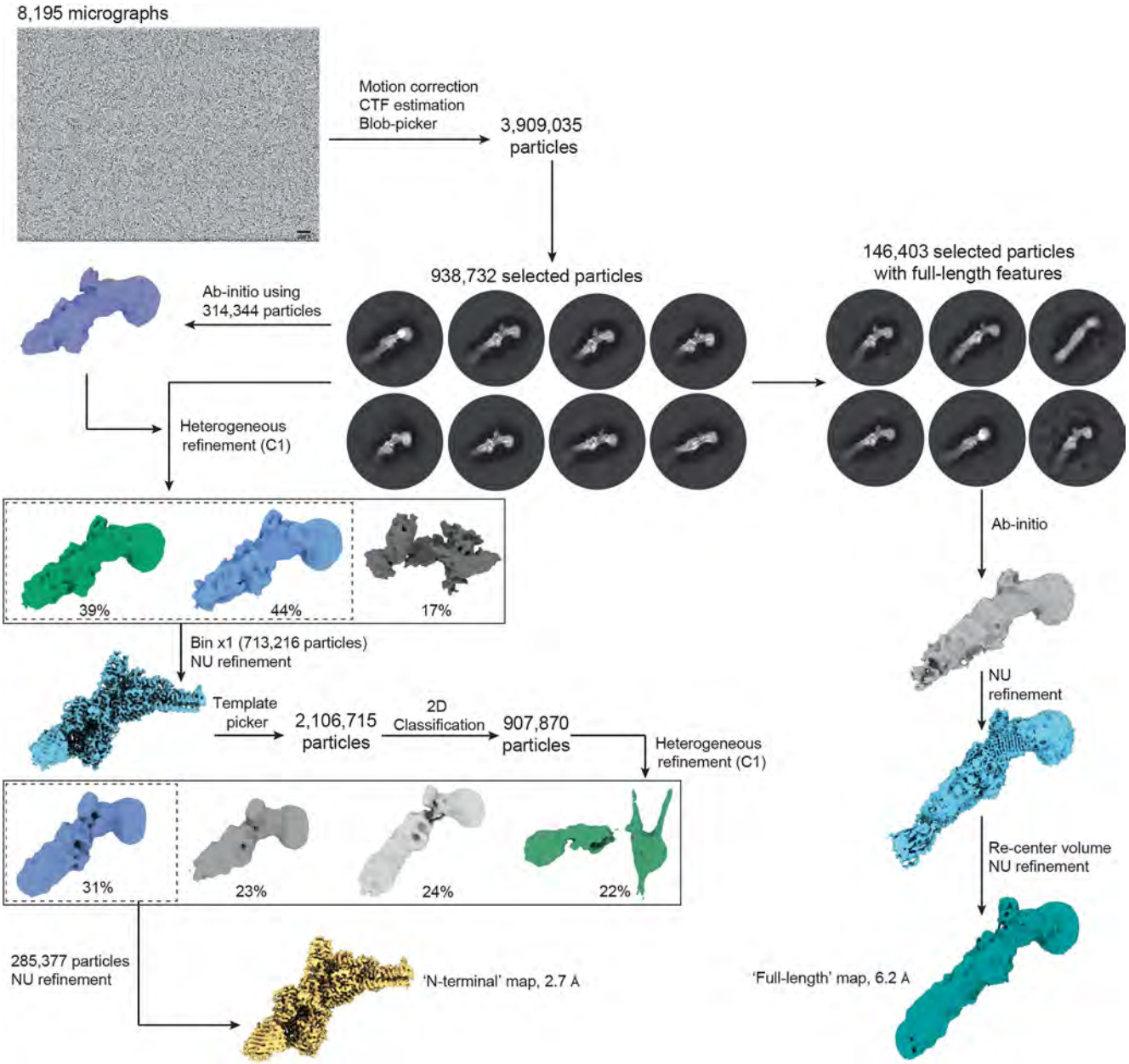

Extended Data Fig. 4 | Cryo-EM data analysis of the LPD-3 complex. Flow chart for cryo-EM data analysis of the LPD-3 "N-terminal" map and "full-length" map. Scale bar of cryo-EM micrograph = 200 Å.

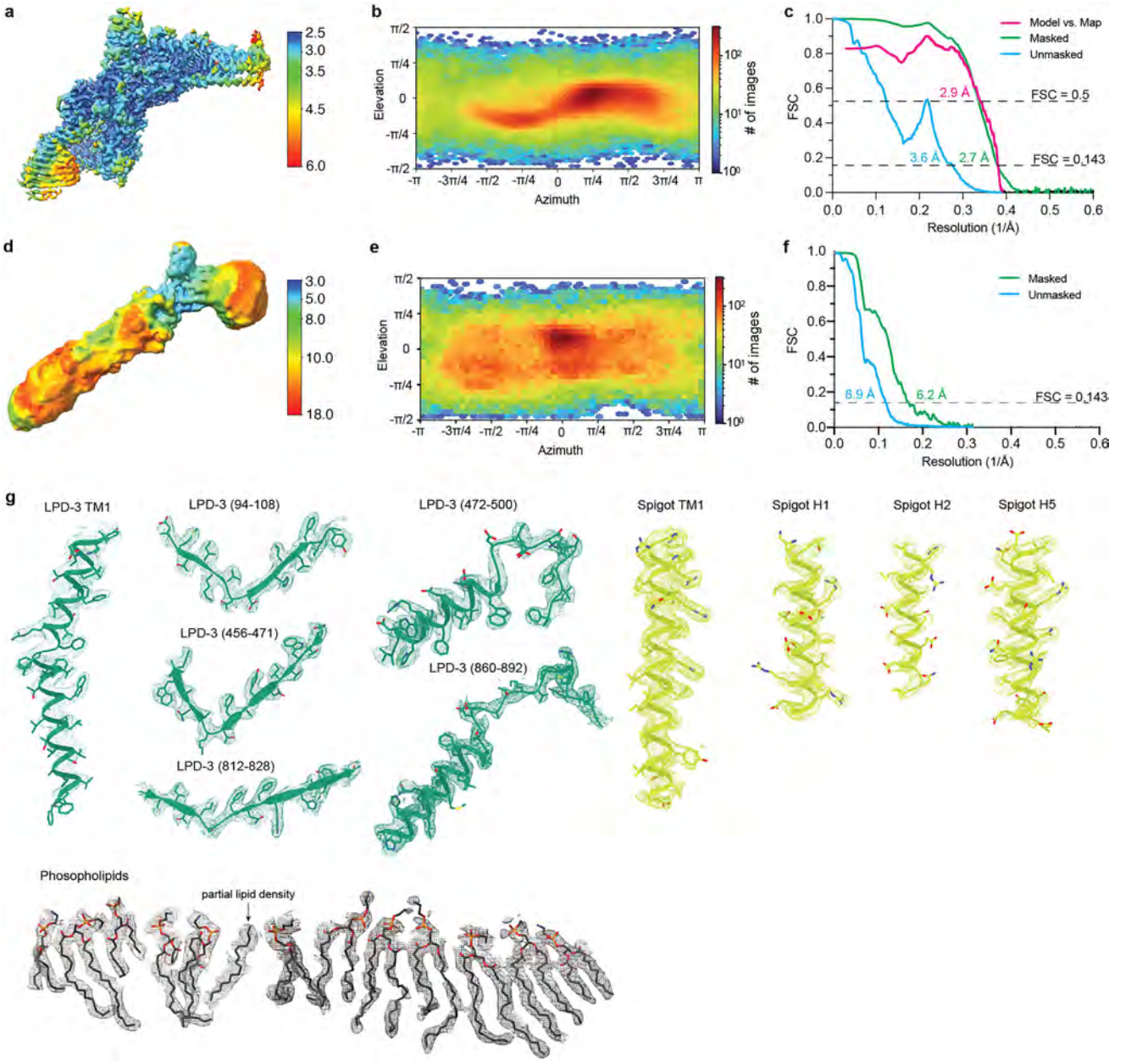

Extended Data Fig. 5 | Cryo-EM statistics, angular distributions, and selected sections of density maps. a, N-terminal cryo-EM density map coloured by local resolution values. **b**, Angular distributions of the final N-terminal reconstruction. **c**, Fourier shell correlations (FSEC) curves for the N-terminal map and model. **d**, Full-length cryo-EM density map coloured by local resolution values. **e**, Angular distributions of the final full-length reconstruction. **f**, Fourier shell correlations (FSEC) curves for the full-length map and model. **g**, Fragments of cryo-EM density map and atomic model of LPD-3, Spigot, and phospholipid molecules in the tunnel. The cryo-EM maps are shown as mesh.

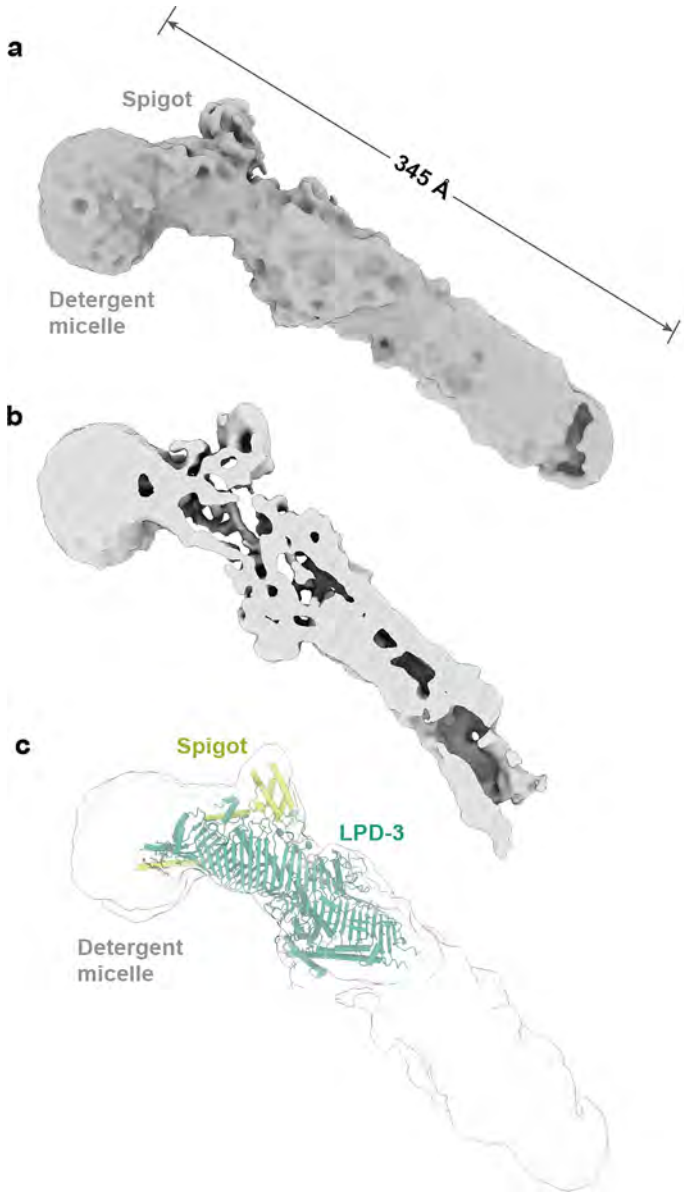

Extended Data Fig. 6 | Cryo-EM density map of the full-length LPD-3 complex. **a**, Cryo-EM density map of the full-length LPD-3 complex, shown parallel to the membrane. **b**, Clipped view of the density map, showing that an internal cavity is observed along the entire length of the map. **c**, A model of the N-terminal LPD-3 complex is fit within the full-length density map. The full-length density map is shown in opaque grey and the model is coloured as in Fig. 1.

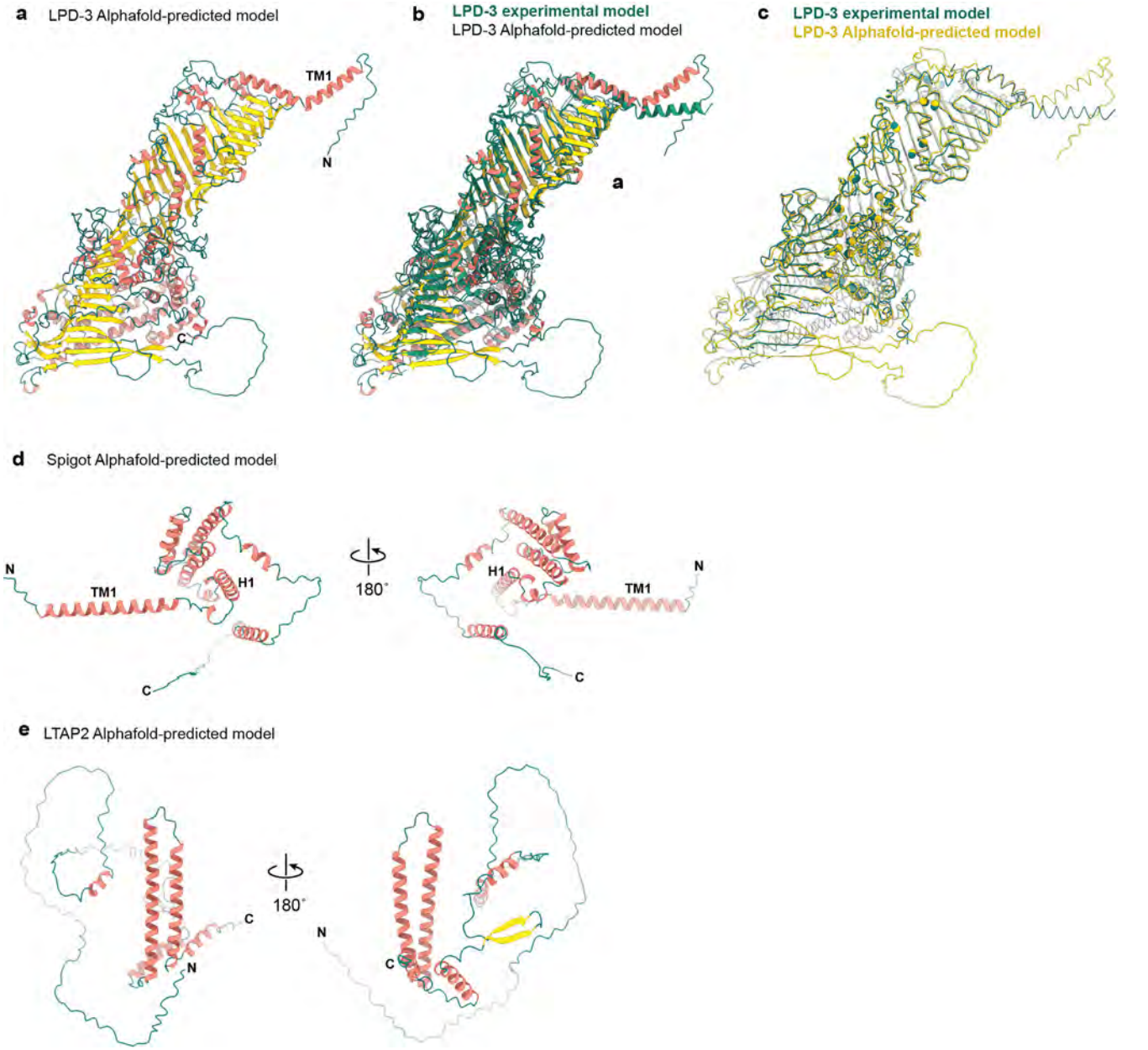

Extended Data Fig. 7 | Alphafold-predicted models of LPD-3 complex subunits. a, The Alphafold-predicted model of LPD-3. β-strands are coloured gold, α-helices are pink, and coils are green. **b**, The Alphafold-predicted structure of LPD-3, coloured as in (a), is superposed on the experimental model of LPD-3 (teal), revealing a high degree of structural similarity. The structures exhibit an overall α-carbon RMSD of 5.6 Å. **c**, The superposed structures of the LPD-3 experimental model (teal) and the Alphafold-predicted structure (gold) are shown in licorice representation. The Cγ atoms of the residues that form the ionizable track are shown as spheres, highlighting the conserved orientation of these residues in the experimental and predicted structures. **d**, The Alphafold-predicted model of Spigot, coloured as in (a). **e**, The Alphafold-predicted model of LTAP2, coloured as in (a).

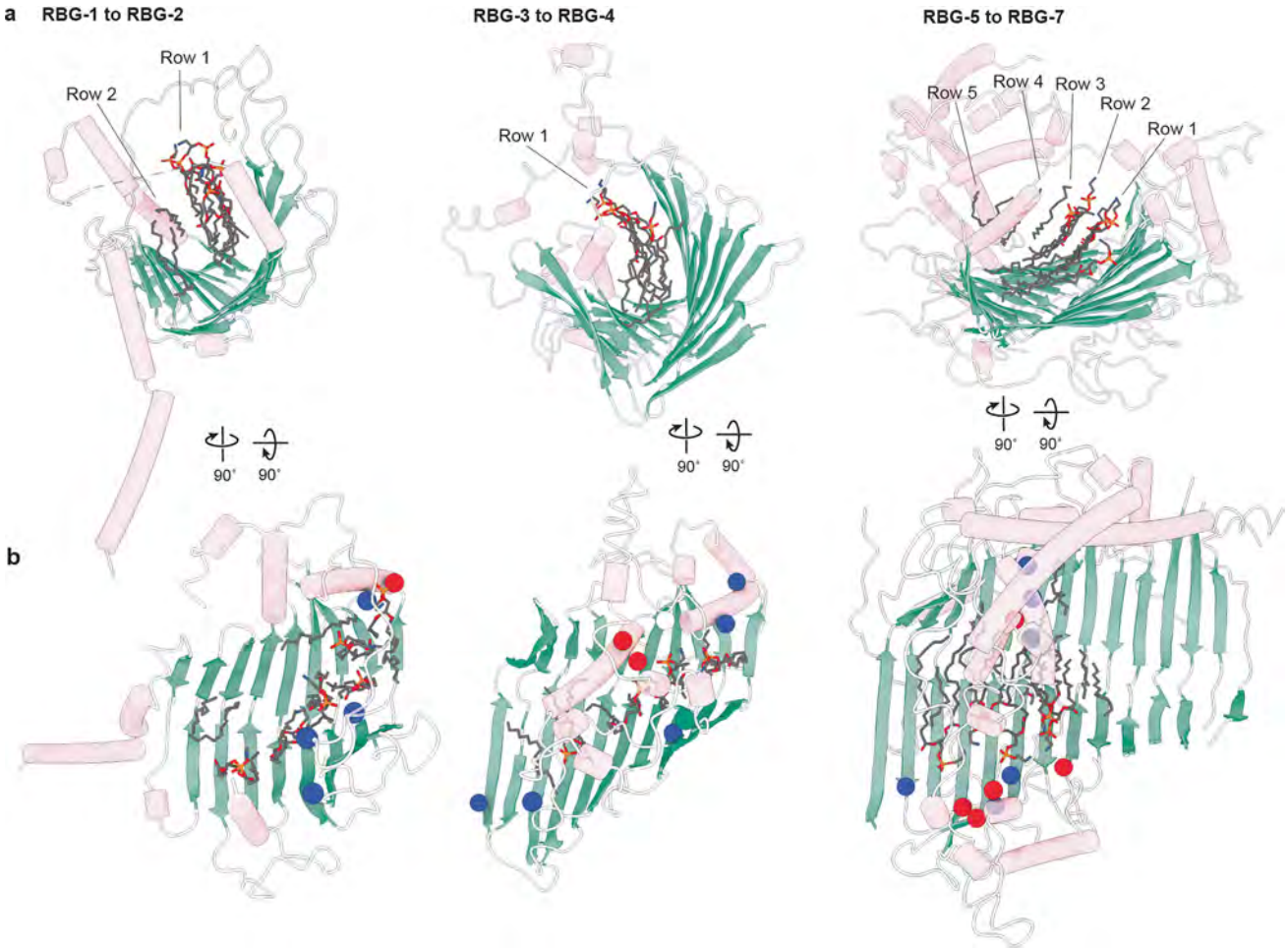

Extended Data Fig. 8 | Lipid organization within the tunnel and the ionizable track. a, Cross sections of the tunnel are shown for the indicated RBG domains to highlight the changes in tunnel width and lipid organization. The protein is coloured according to secondary structure element: α-helices are pink, loops are white, and β-strands are teal. Lipids are shown as grey sticks. **b**, 90° rotated view of the indicated RBG domains shows the organization of lipids, as well as the locations of ionizable residues within the LPD-3 tunnel. Basic resides are shown as blue spheres and acidic residues are shown as red spheres. Other structural elements are coloured as in (a).

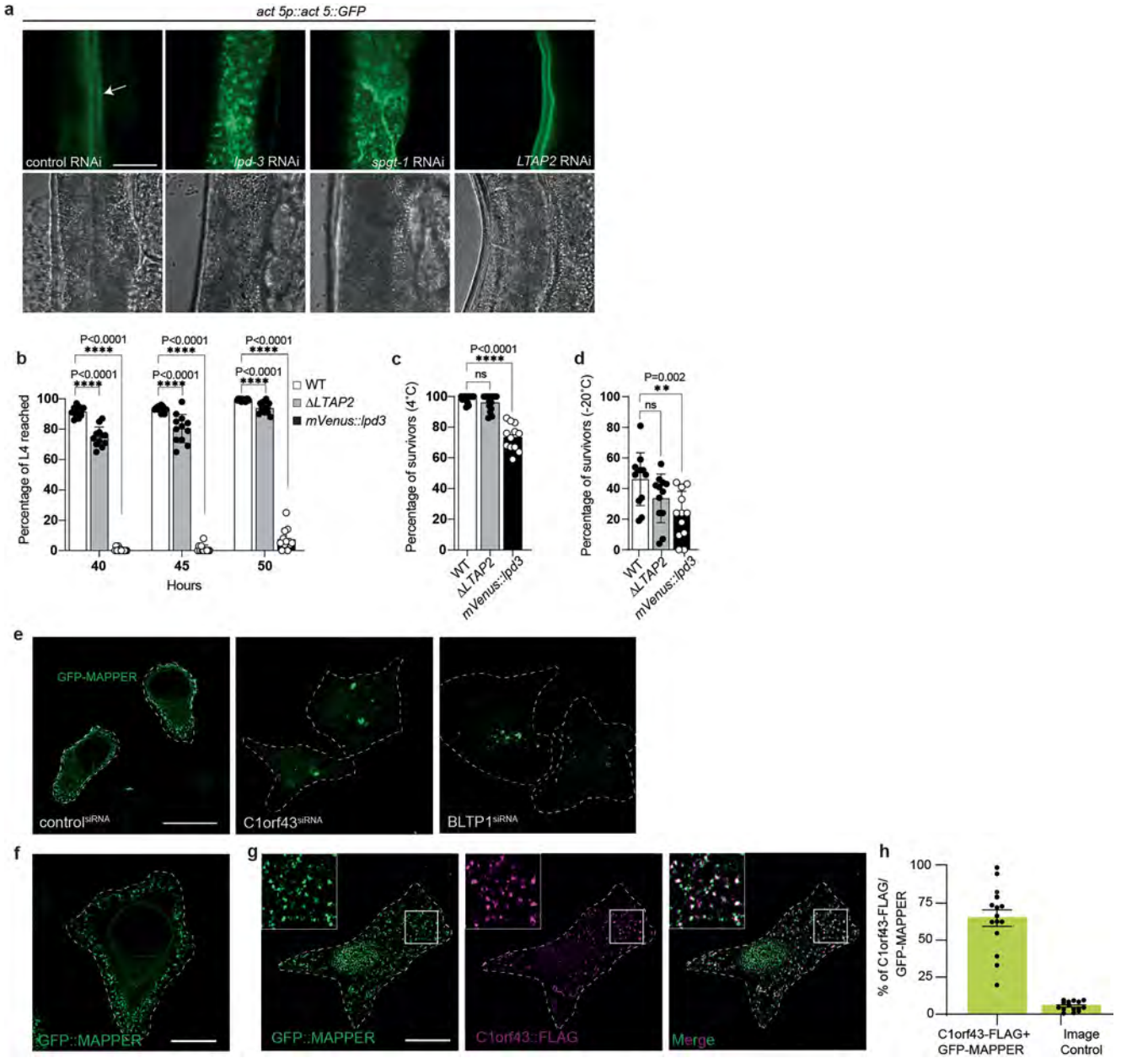

Extended Data Fig. 9 | Knockdown of *spgt-1* and *LTAP2*. **a**, Representative confocal fluorescence images showing the actin reporter *act5p::act-5::GFP* in wildtype *C. elegans* and *C. elegans* that were treated with RNAi targeting *lpd-3*, *spgt-1*, or *LTAP2*. Corresponding brightfield images are shown below each GFP fluorescence image. The apical intestinal membrane is indicated with an arrow. N = 24 worms were imaged for each condition. Scale bar is 20 µm. For the sequences of each RNAi construct, see Supplementary Table 1. **b**, Percentages of animals that reached developmental L4 stage at indicated hours post egg preparation in wild type (WT) worms, *ΔLTAP2* worms, or *mVenus::lpd3* worms. Values are means +/− S.D. **c**, Percentages of L4 stage animals that survived cold exposure (4 °C for 20 h) in wild type (WT) worms, *ΔLTAP2* worms, or *mVenus::lpd3* worms. Values are means +/− S.D. **d**, Percentages of L4 stage animals that survived freeze exposure (−20 °C for 45 min) in wild type (WT) worms, *ΔLTAP2* worms, or *mVenus::lpd3* worms. Values are means +/− S.D. *P < 0.05, **P < 0.01, ****P < 0.0001 (two-sided unpaired t-test, N = 12 biological replicates for all experiments in (b), (c), and (d)). **e**, Knockdown of endogenous *C1orf43* or *BLTP1* with siRNA leads to ER-PM contact site collapse as visualized by GFP::MAPPER. Cells are outlined with white dashed lines. Scale bar is 20 µm. N = 15 cells were imaged for each condition. **f**, Representative confocal microscopy image of a HeLa cell expressing GFP::MAPPER to mark ER-PM contact sites. Scale bar = 10 µm. **g**, Representative confocal microscopy images of a HeLa cell co-expressing GFP::MAPPER and C1orf43::FLAG, showing robust colocalization. Mislocalization of GFP::MAPPER, a potential indicator of cellular stress, is evident when the leftmost image is compared to (**f**). Cells are outlined with white dashed lines. Scale bar = 10 µm. **h**, Quantitation of the co-localization between GFP::MAPPER and C1orf43::FLAG. N = 15 biological replicates for both samples. Data are presented as mean values +/− S.E.M.

Extended Data Table 1 | Statistics for 3D reconstruction and model refinement

Codes	PDB 9CAP EMD-43599 (N-terminal) EMD-45276 (full-length)
Data collection and processing	
Microscope	Titan Krios
Camera	K3 BioQuantum
Magnification	29,000
Voltage (kV)	300
Defocus range (μm)	-1.5 to -2.5
Exposure time (s)	5.19
Dose rate ($e^-/Å^2/s$)	7.98
Number of frames	50
Pixel size (Å)	0.788 (0.394 super-resolution)
Micrographs (no.)	8,195
Symmetry imposed	C1
Initial particles (no.)	3,909,035
Final particles (no.)	285,377 (N-terminal), 146,403 (full-length)
Map resolution (Å)	2.7 (N-terminal, 6.2 (full-length)
FSC threshold	0.143
Refinement	
Initial model	Alphafold
Model resolution (Å)	2.9
FSC threshold	0.5
Model composition	
Non-hydrogen atoms	13,789
Protein atoms	12,910
Ligand atoms	879
B factors ($Å^2$)	
Protein	30.0
Lipids	59.8
R.m.s. deviations	
Bond length (Å)	0.012
Bond angle (°)	1.481
Validation	
Favored (%)	97.5
Allowed (%)	2.5
Disallowed (%)	0
Poor rotamers (%)	0.21
MolProbity score	1.51
Clash score	7.36

nature portfolio

Corresponding author(s): Sarah Clark

Last updated by author(s): March 14, 2025

Reporting Summary

Nature Portfolio wishes to improve the reproducibility of the work that we publish. This form provides structure for consistency and transparency in reporting. For further information on Nature Portfolio policies, see our Editorial Policies and the Editorial Policy Checklist.

Statistics

For all statistical analyses, confirm that the following items are present in the figure legend, table legend, main text, or Methods section.

n/a	Confirmed
☐	☒ The exact sample size (*n*) for each experimental group/condition, given as a discrete number and unit of measurement
☐	☒ A statement on whether measurements were taken from distinct samples or whether the same sample was measured repeatedly
☐	☒ The statistical test(s) used AND whether they are one- or two-sided *Only common tests should be described solely by name; describe more complex techniques in the Methods section.*
☒	☐ A description of all covariates tested
☐	☒ A description of any assumptions or corrections, such as tests of normality and adjustment for multiple comparisons
☐	☒ A full description of the statistical parameters including central tendency (e.g. means) or other basic estimates (e.g. regression coefficient) AND variation (e.g. standard deviation) or associated estimates of uncertainty (e.g. confidence intervals)
☐	☒ For null hypothesis testing, the test statistic (e.g. *F*, *t*, *r*) with confidence intervals, effect sizes, degrees of freedom and *P* value noted *Give P values as exact values whenever suitable.*
☒	☐ For Bayesian analysis, information on the choice of priors and Markov chain Monte Carlo settings
☒	☐ For hierarchical and complex designs, identification of the appropriate level for tests and full reporting of outcomes
☒	☐ Estimates of effect sizes (e.g. Cohen's *d*, Pearson's *r*), indicating how they were calculated

Our web collection on statistics for biologists contains articles on many of the points above.

Software and code

Policy information about availability of computer code

Data collection	Cryo-EM: SerialEM 3.8; Microscopy: ZEN 2.3 SP1 FP1 (Black Edition, version 14.0.9.201) and ZEN 2.3 (Blue Edition, version 2.3.69.1013)
Data analysis	Cryo-EM: CryoSparc 3.3.1, ChimeraX 1.7.1, PHENIX 1.21, COOT 0.9.8.92, Alphafold2; Mass spectrometry: Comet v.2016.01; Statistical analysis: Graphpad Prism 9

For manuscripts utilizing custom algorithms or software that are central to the research but not yet described in published literature, software must be made available to editors and reviewers. We strongly encourage code deposition in a community repository (e.g. GitHub). See the Nature Portfolio guidelines for submitting code & software for further information.

Data

Policy information about availability of data

All manuscripts must include a data availability statement. This statement should provide the following information, where applicable:

- Accession codes, unique identifiers, or web links for publicly available datasets
- A description of any restrictions on data availability
- For clinical datasets or third party data, please ensure that the statement adheres to our policy

The volumes for the cryo-EM data have been deposited in the Electron Microscopy Data Bank under accession codes EMD-45276 (full-length) and EMD-45399 (N-terminal). The coordinates of the LPD-3 complex have been deposited in the Protein Data Bank under accession code 9CAP. Source data are provided with this

paper. The full version of the silver stain gel is included in SI Fig 1 and the sequences for all RNAi constructs are included in SI Figs 2-3. Uniprot accession number for LPD-3: A0A0K3AWP8. Uniprot accession number for Spigot: Q4W5H0. Uniprot accession number for LTAP2: U4PLN7.

Research involving human participants, their data, or biological material

Policy information about studies with human participants or human data. See also policy information about sex, gender (identity/presentation), and sexual orientation and race, ethnicity and racism.

Reporting on sex and gender	Human participants, their data, or human biological material were not used in this study.
Reporting on race, ethnicity, or other socially relevant groupings	*Please specify the socially constructed or socially relevant categorization variable(s) used in your manuscript and explain why they were used. Please note that such variables should not be used as proxies for other socially constructed/relevant variables (for example, race or ethnicity should not be used as a proxy for socioeconomic status).* *Provide clear definitions of the relevant terms used, how they were provided (by the participants/respondents, the researchers, or third parties), and the method(s) used to classify people into the different categories (e.g. self-report, census or administrative data, social media data, etc.)* *Please provide details about how you controlled for confounding variables in your analyses.*
Population characteristics	*Describe the covariate-relevant population characteristics of the human research participants (e.g. age, genotypic information, past and current diagnosis and treatment categories). If you filled out the behavioural & social sciences study design questions and have nothing to add here, write "See above."*
Recruitment	*Describe how participants were recruited. Outline any potential self-selection bias or other biases that may be present and how these are likely to impact results.*
Ethics oversight	*Identify the organization(s) that approved the study protocol.*

Note that full information on the approval of the study protocol must also be provided in the manuscript.

Field-specific reporting

Please select the one below that is the best fit for your research. If you are not sure, read the appropriate sections before making your selection.

☒ Life sciences ☐ Behavioural & social sciences ☐ Ecological, evolutionary & environmental sciences

For a reference copy of the document with all sections, see nature.com/documents/nr-reporting-summary-flat.pdf

Life sciences study design

All studies must disclose on these points even when the disclosure is negative.

Sample size	No statistical methods were used to predetermine sample size. Sample sizes of cryo-EM data were determined by the availability of the microscope time. Sample size for spectral confocal imaging of worms was determined based on consistency between samples and published studies (e.g. Wang et al. 2022, Nat. Comm. 6805). Sample size for co-localization experiments in HeLa cells was determined based on the transfection consistency of the the fluorescent marker. Sample size for RNAi-mediated knockdown experiments in Drosophila astrocytes and C. elegans was determined based on experimental trials and previously published studies (Kang et al. 2023, BioRxiv, doi: https://doi.org/10.1101/2023.11.06.565932). Sample size for cold tolerance and development assays of transgenic C. elegans strains was determined based on published studies (Wang et al. 2022, Nat. Comm. 6805).
Data exclusions	The following exclusions were pre-established. Particles were removed if their 3D reconstructions had poor quality.
Replication	All experiments were performed with independent replicates as described and replicates were successful within expected variation. Cryo-EM related experiments, including protein purification, were successfully reproduced at least two times independently. Spectral confocal images of ten worms of different larval and adult stages were collected in two separate experiments and yielded identical results. Mass spectrometry experiments were not replicated because a control sample of identically-prepared wildtype worms was analyzed concurrently with the transgenic worm sample. Co-localization experiments in HeLa cells were replicated two times. siRNA experiments were replicated two times. RNAi-mediated knockdown experiments were replicated two times. Cold tolerance and developmental assays were collected in four separate experiments on different days and yielded statistically similar results.
Randomization	For studies involving Drosophila, C. elegans, or cultured cells, the animal or cell was randomly chosen from the vial or plate for downstream behavioral or imaging experiments. Randomization is not relevant to the biochemical and structural experiments described in this work because these experiments did not involve allocating discrete samples to experimental groups.
Blinding	For the RNAi screen in Drosophila, the researchers were blinded regarding the target gene of each RNAi. For structural, biochemical, and microscopy studies, investigators were not blinded because knowledge of the sample does not impact the measurement of these data.

Reporting for specific materials, systems and methods

We require information from authors about some types of materials, experimental systems and methods used in many studies. Here, indicate whether each material, system or method listed is relevant to your study. If you are not sure if a list item applies to your research, read the appropriate section before selecting a response.

Materials & experimental systems

n/a	Involved in the study
☐	☒ Antibodies
☐	☒ Eukaryotic cell lines
☒	☐ Palaeontology and archaeology
☐	☒ Animals and other organisms
☒	☐ Clinical data
☒	☐ Dual use research of concern
☒	☐ Plants

Methods

n/a	Involved in the study
☒	☐ ChIP-seq
☒	☐ Flow cytometry
☒	☐ MRI-based neuroimaging

Antibodies

Antibodies used

anti-Crz (produced for this study, used at 1:500 dilution), anti-GFP (RRID:AB_300798, Abcam, Cat #ab13970, used at 1:1000), anti-FLAG (RRID:AB_1625982, Sigma-Aldrich, Cat #F3165, used at 1:250 dilution), Cy3-conjugated AffiniPure Goat Anti-rabbit IgG (H+L) secondary antibody (Jackson Immunoresearch, Cat#111-165-003, used at 1:500 dilution)

Validation

Anti-Crz antibody: We used a rabbit polyclonal antibody that was produced for this study (see Methods section). The antibody was validated by checking the staining pattern in the Drosophila central nervous system, as described in the Method section. The pattern was similar to previous reports and co-staining with Crz-Gal4; UAS-mCD8::GFP showed complete colocalization.
Anti-GFP Antibody: We used a chicken polyclonal anti-GFP antibody (Abcam, Cambridge, MA, Cat# ab13970, used at a 1:1000 dilution for immunofluorescence). The specificity of this antibody was demonstrated in cell culture by using negative and positive control conditions. The positive controls replicated previously reported data and the negative controls exhibited no staining. We further validated it by confirming its ability to detect GFP-tagged proteins in Drosophila tissues. Further validation can be found on the manufacturer's website:
https://www.abcam.com/en-us/products/primary-antibodies/gfp-antibody-ab13970
Anti-FLAG Antibody: We used a mouse monoclonal anti-FLAG antibody (Sigma-Aldrich, St. Louis, MO, Cat# F3165, used at a 1: 250 for immunofluorescence. This antibody has been widely validated for detecting FLAG-tagged proteins, as seen in the manufacturer's website (below), and we further confirmed its specificity by detecting FLAG-tagged Tweek in Drosophila tissues.
https://www.sigmaaldrich.com/US/en/product/sigma/f3165?
utm_source=google&utm_medium=cpc&utm_campaign=22180208315&utm_content=179433150372&gad_source=1&gclid=CjwKCAiAlPu9BhAjEiwA5NDSAys_f-k4Gb9cNy2aI6jPqV30iEXDPpv3pxJxnDAsfgPsOk93pFU1sRoCq-4QAvD_BwE

Eukaryotic cell lines

Policy information about cell lines and Sex and Gender in Research

Cell line source(s)

HeLa Cells (RRID:CVCL_0030) were obtained from ATCC.

Authentication

Cells were not authenticated.

Mycoplasma contamination

Cells tested negative for mycoplasma contamination using Hoechst 33258 staining.

Commonly misidentified lines
(See ICLAC register)

No commonly misidentified cell lines were used in this study.

Animals and other research organisms

Policy information about studies involving animals; ARRIVE guidelines recommended for reporting animal research, and Sex and Gender in Research

Laboratory animals

Transgenic C. elegans were generated by SunyBiotech (strains: PHX5024 lpd-3 (syb5024), PHX5131 lpd-3 (syb5131), and strain PHX9850 Y38C1AA.12a(syb9850)). Worms of mixed larval and adult ages were grown and maintained in an incubator set at 20C. D. melanogaster were dissected at wandering larva stages (wL3) and head eversion (HE), a developmental stage that occurs approximately 12 hours into metamorphosis. The following D. melanogaster strains were used: GMR25H07-Gal4 (Bloomington, 49145), UAS-FLP5.DD, UAS- tweek RNAi (VDRC 110686), CG6665 RNAi (Bloomington 60402), CG10874 RNAi (NIG-Fly, 10874R-3, Pepck2 RNAi (VDRC 107092), Apoltp RNAi (Bloomington 51937), CG33303 RNAi (VDRC 107778), FASN1 RNAi (VDRC 108339), SERCA RNAi (VDRC 107446), SdhA RNAi (VDRC 110440), Rack1 RNAi (VDRC 104470), PCB RNAi (VDRC 105936), Rab1 RNAi (Bloomington 27299), Idh RNAi (VDRC 100554).

Wild animals

The study did not involve wild animals.

Reporting on sex

Sex was not considered in the study design for C. elegans or D. melanogaster experiments. The vast majority of C. elegans are hermaphrodites and a small percentage (<0.2%) are males. Female and male D. melanogaster animals were used for RNAi-mediated knockdown experiments.

Field-collected samples	No field-collected samples were used in this study.
Ethics oversight	C. elegans or D. melanogaster experiments do not require ethical approval.

Note that full information on the approval of the study protocol must also be provided in the manuscript.

Plants

Seed stocks	Plants were not used in this study.
Novel plant genotypes	*Describe the methods by which all novel plant genotypes were produced. This includes those generated by transgenic approaches, gene editing, chemical/radiation-based mutagenesis and hybridization. For transgenic lines, describe the transformation method, the number of independent lines analyzed and the generation upon which experiments were performed. For gene-edited lines, describe the editor used, the endogenous sequence targeted for editing, the targeting guide RNA sequence (if applicable) and how the editor was applied.*
Authentication	*Describe any authentication procedures for each seed stock used or novel genotype generated. Describe any experiments used to assess the effect of a mutation and, where applicable, how potential secondary effects (e.g. second site T-DNA insertions, mosiacism, off-target gene editing) were examined.*